fluids

MDPI

Article

A Unified Drift–Flux Framework for Predictive Analysis of Flow Patterns and Void Fractions in Vertical Gas Lift Systems

Omid Heydari, Sohrab Zendehboudi and Stephen Butt *

Department of Process Engineering, Memorial University of Newfoundland, St. John's, NL A1C 5S7, Canada; oheydari@mun.ca (O.H.); szendehboudi@mun.ca (S.Z.)
* Correspondence: sdbutt@mun.ca

Abstract

This study utilizes the drift–flux model to develop a new flow pattern map designed to facilitate an accurate estimation of gas void fraction (α_g) in vertical upward flow. The map is parameterized by mixture velocity (u_m) and gas volumetric quality (β_g), integrating transition criteria from the established literature. For applications characterized by significant pressure gradients, such as gas lift, these criteria were reformulated as functions of pressure, enabling direct estimation from operational data. A critical component of this methodology for the estimation of α_g is the estimation of the distribution parameter (C_0). An analysis of experimental data, spanning pipe diameters from 1.27 to 15 cm across the full void fraction ranges ($0 < \alpha_g < 1$), reveals a critical α_g threshold beyond which C_0 exhibits a distinct decreasing trend. To characterize this phenomenon, the parameter of the distribution-weighted void fraction ($\alpha_c = \alpha_g C_0$) is introduced. This parameter, representing the dynamically effective void fraction, identifies the critical threshold at its inflection point. The proposed model subsequently defines C_0 using a two-part function of α_c. This generalized approach simplifies the complexity inherent in existing correlations and demonstrates superior predictive accuracy, reducing the average error in α_g estimations to 5.4% and outperforming established methods. Furthermore, the model's parametric architecture is explicitly designed to support the optimization and fine-tuning of coefficients, enabling future use of machine learning for various fluids and complex industrial cases.

Keywords: two-phase flow; drift–flux; gas lift; void fraction; distribution parameter; flow pattern

Check for updates

Academic Editors: Wenning Zhou, Faik Hamad and Priscilla Ribeiro Varges

Received: 4 November 2025
Revised: 15 December 2025
Accepted: 19 December 2025
Published: 26 December 2025

Copyright: © 2025 by the authors. Licensee MDPI, Basel, Switzerland. This article is an open access article distributed under the terms and conditions of the Creative Commons Attribution (CC BY) license.

1. Introduction

The simultaneous flow of gas and liquid through a conduit is a phenomenon central to a vast array of industrial processes. Characterizing this complex flow depends on dynamic properties of the flow, such as velocities and mixture densities, which are affected by gas void fraction, the most fundamental governing parameter [1,2]. Its accurate estimation is not merely an academic exercise but a critical prerequisite for the safe design, efficient operation, and reliable analysis of systems across the nuclear, petroleum, and chemical processing industries [1].

The volumetric void fraction of gas is frequently employed in experimental measurements, and it is used in numerical simulations employing Finite Volume Methods (FVMs) within computational cells. The gas void fraction (α_g) is mathematically defined as the

ratio of the volume occupied by the gaseous phase (V_g) to the total volume occupied by the mixture (V_m) as given below:

$$\alpha_g = \frac{V_g}{V_m} \tag{1}$$

The inherent slip, or relative velocity, between the lighter, faster-moving gas phase and the denser liquid phase presents a significant modeling challenge for the estimation of void fractions of phases. Over the decades, several modeling approaches have emerged to tackle this challenge. These range from simple empirical correlations and slip ratio models to the more physically robust and widely adopted drift–flux model [3]. The success of any model is measured by its ability to provide accurate predictions across a wide range of operating conditions, fluid properties, and pipe geometries. One of the simpler approaches is the Homogeneous Equilibrium Model (HEM), which assumes no slip between the phases, and while computationally trivial, this assumption is rarely valid in vertical upward flow, where buoyancy effects are significant, often leading to considerable inaccuracies [4]. A general equation was proposed by Butterworth to consider the effects of liquid properties on gas void fraction (Equation (2)) [5].

$$\alpha_g = \frac{1}{1 + S\left(\frac{1-x}{x}\right)\left(\frac{\rho_g}{\rho_l}\right)} \tag{2}$$

The term x represents the gas quality, ρ_l and ρ_g introduce the liquid and gas densities, respectively, and the term S stands for the ratio of average gas velocity to average liquid velocity. There are various empirical correlations for the slip term, which are functions of parameters such as gas quality, density, and viscosity ratios in models such as Fauske, Zivi, Spedding and Chen, and Hamersma and Hart [6–9]. Some models, like Chisholm's correlation and Smith's correlation, found term S as a parameter and function of gas quality and density ratios [10,11]. These approaches are easy to use and straightforward; however, their application range is limited to specific conditions, thus, they need to be refined to make them applicable to specific cases.

The modeling of two-phase flow presents a fundamental trade-off between physical fidelity and computational feasibility [12]. The simplest form of modeling is the HEM, which assumes both phases to move at the same velocity, a simplification that is often inaccurate for flow systems with significant slip [4]. At the other end is the numerical solution to momentum and continuity equations, like Computational Fluid Dynamics (CFD). While mechanistically detailed, this approach includes many closure relationships for interfacial transfer terms (mass, momentum, and energy), which are often complex, uncertain, and a source of numerical instability [13]. The Drift Flux Model (DFM) introduces a critical middle ground, offering a more sophisticated representation of phase slip than the HEM while avoiding the full complexity of solving continuity and momentum equations [14].

The core strength of the DFM is its treatment of the two-phase mixture as a single fluid with its own mixture properties. The model is formulated based on a single momentum conservation equation for the mixture, which greatly simplifies the mathematical system and is widely used as a base for the estimation of two-phase velocities and void fraction distributions. The DFM's theoretical framework is built on the relationship between area-averaged volumetric flux and phase velocities, which is defined by two key parameters: the distribution parameter (C_0), accounting for non-uniform velocity and phase concentration profiles, and the drift velocity (u_d), which addresses kinematic non-equilibrium [14–19]. The general representation of the DFM, which represents the relation between actual gas velocity (u_g) and mixture velocity (u_m), is as follows [14]:

$$u_g = C_0 u_m + u_d \tag{3}$$

To better understand how these terms are being defined and how they are affecting the system, it is crucial to understand what values to expect for C_0 and u_d terms.

u_m introduces the area-averaged mixture volumetric flux, which is equal to the summation of superficial velocities of each phase $(u_{sl} + u_{sg})$. In other words, the parameter introduces the total volume of mixture passing through a unit area per time. C_0 accounts for the effects of non-uniform radial profiles of both α_g and u_m across the pipe's cross-section, and it physically represents the covariance of the radial profiles of the void fraction and velocity [14]. In a typical turbulent pipe flow, the velocity profile peaks at the center. If the gas bubbles also tend to concentrate in this high-velocity central region, the gas phase is transported more effectively than the mixture average, resulting in a value of $C_0 > 1$, and for dispersed two-phase flows that have moved beyond the simple bubbly regime, the asymptotic value of the distribution parameter is commonly accepted to be approximately 1.2 for upward flows in pipes [17,18,20,21].

u_d represents the velocity of the gas phase relative to the mixture volumetric flux. It quantifies the local slip between the phases, which is primarily driven by the balance of local forces, most notably buoyancy (due to density differences) and hydrodynamic drag. This parameter captures the tendency of lighter gas bubbles to rise through the denser surrounding liquid, independent of the bulk motion of the mixture [14,21].

In simpler words, the DFM, formulated by Zuber–Findlay, separates two distinct contributions to phase slip: the global, profile-driven term represented by C_0 and the local, force-balance-driven term represented by u_d [14]. This model was developed under the assumption of constant phase densities and no phase change in the control volume, which makes it applicable to adiabatic, two-component flows systems [14]. While the DFM provides a robust theoretical framework, its predictive accuracy is entirely contingent on the quality of the empirical or semi-empirical closure correlations used for these two parameters, but it is still a popular choice because it effectively balances predictive accuracy with computational simplicity [17,18,22].

There are different models developed based on the DFM, and the differences between the models are mostly in the values of C_0 and u_d, which are listed in Table 1. However, their validity is often confined to the specific range of fluid properties, pipe diameters, pressures, and flow patterns for which they were developed. For instance, some DFM methods developed for either very small or very large pipes often fail to adequately model the distinct flow structures, particularly the stability of large bubbles, observed in medium-diameter channels [23,24]. Furthermore, some correlations perform well for bubbly flow but do not provide a good accuracy for annular flow, and vice versa [25]. For example, the correlation by Nicklin et al., a simple and popular model, shows acceptable performance for bubbly and slug flow systems but is unsatisfactory at high void fractions typical of annular flow [26,27]. Conversely, some annular flow models are inappropriate for dispersed flows. This dependency necessitates a priori knowledge of the flow pattern to select the appropriate correlation, which is a practical limitation, as the flow pattern itself is an outcome of the flow conditions. There were several attempts to create full-range correlations aimed to overcome this issue by providing continuous functions across all regimes, but they often rely on extensive curve fitting, which can sometimes obscure the underlying physics [28]. Moreover, models derived from data fitting procedures are susceptible to a compensation error, where an inaccuracy in determining one parameter (e.g., C_0) is mathematically compensated by an error in the other (e.g., u_d), leading to a parameter set that fits the data but may lack a firm physical basis [29]. Also, full-range models are often developed analytically based on a consistency principle, which assumes

that theoretical velocity and void fraction profiles hold true across dispersed, transition, and separated flow regimes [18]. A comparative study on 52 models was performed by Godbole et al., and the accuracy of several models in different void fraction zones and various flow patterns was analyzed. They found limitations of void fraction predictions for some of the better-performing models, like the Nicklin et al. model, in gas void fractions above 0.75 [3].

Contemporary research has largely focused on overcoming the limitations of conventional DFM correlations, which are often not applicable over wide-ranging flow conditions or fail to capture complex flow physics accurately [18,30]. Dependency on the flow pattern, a specific range of α_g, or complex empirical correlations is a major shortcoming of models, which creates the need for genuinely full-range DFM models [18,30]. Another key issue is the inaccurate modeling of distribution parameters in developing flows. While these DFM closure parameters are typically assumed to be constant in the fully developed region, this assumption breaks down where flow profiles are actively evolving [17].

Different models rely on a set of core assumptions, like specific operating conditions for key parameters of the drift–flux relationship, such as u_d and C_0, to characterize phase velocity differences and the void fraction [18,19]. To mechanistically model transitions between flow regimes, particularly the shift from dispersed to slug flow, a two-group bubble approach is frequently adopted, which classifies bubbles into small, dispersed (group-one) and large, cap/slug (group-two) types, a framework that aids in the analytical derivation of DFM parameters across these transitions [23,31].

Recent research has significantly advanced the DFM for estimating two-phase flow features across various pipe sizes and conditions. Hibiki and Tsukamoto developed a drift velocity model for the bubbly to beyond-bubbly transition in medium to large diameter pipes (5.08 to 30.5 cm) using a two-group approach to predict non-monotonic velocity behavior [31]. Expanding the model's scope, Hibiki et al. analytically derived a full-range DFM correlation for vertical pipes (diameters of 0.6 to 6.7 cm) that spans dispersed, transition, and separated flows [18]. Specific applications have also been refined. For subcooled boiling in small diameter pipes (0.975 to 2.4 cm), Dong and Hibiki created a new void fraction model by pairing a flow quality model with the full-range DFM to improve axial profile predictions [32]. Song and Hibiki proposed a two-group DFM for medium-sized diameter pipes (1.27 to 5.08 cm) [23]. Finally, Nepomnyashchikh and Liburdy experimentally demonstrated that DFM parameters behave nonlinearly in a flow's developing region, only reaching conventional asymptotic values as the flow fully develops [17].

Although in some specific cases, the highest precision of predictions may be required, in applications such as gas lift, simplicity of models is preferred over an extreme precision offered by complicated models since operational conditions in long vertical pipes vary significantly, and dependency on case-specific models can cause more challenges and inaccuracies. Table 1 shows some of the simplified models for estimation of DFM parameters in which σ is the surface tension between the gas and liquid phase, g represents the acceleration due to gravity, and Re is the Reynolds number.

Table 1. Example of models representing the distribution parameter and the drift velocity for the DFM.

Model	Distribution Parameter	Drift Velocity	
Nicklin et al. [26]	$C_0 = 1.2$	$u_d = 0.35\sqrt{gD}$	(4)
Zuber and Findlay [1] [14]	$C_0 = 1.2$	$u_d = 1.53\left[g\sigma\left(1-\frac{\rho_g}{\rho_l}\right)\right]^{0.25}$	(5)
Bonnecaze et al. [33]	$C_0 = 1.2$	$u_d = 0.35\sqrt{gD}\left(1-\frac{\rho_g}{\rho_l}\right)$	(6)
Greskovich and Cooper [34]	$C_0 = 1.0$	$u_d = 0.671\sqrt{gD}$	(7)
Ishii [2] [16]	$C_0 = 1.2 - 0.2\left(\frac{\rho_g}{\rho_l}\right)^{0.5}\left(1-e^{-18\alpha_g}\right)$	$u_d = (C_0-1)u_m + \sqrt{2}\left[g\sigma\left(1-\frac{\rho_g}{\rho_l}\right)\right]^{0.25}$	(8)
Pearson et al. [35]	$C_0 = 1 + 0.796e^{-(0.061\sqrt{\frac{\rho_g}{\rho_l}})}$	$u_d = 0.034\left(\sqrt{\frac{\rho_g}{\rho_l}}-1\right)$	(9)
Liao et al. [3] [36]	$C_0 = 1.2 - 0.2\left(\frac{\rho_g}{\rho_l}\right)^{0.5}\left(1-e^{-18\alpha_g}\right)$	$u_d = 0.33\left[g\sigma\left(1-\frac{\rho_g}{\rho_l}\right)\right]^{0.25}$	(10)
Morooka et al. [37]	$C_0 = 1.08$	$u_d = 0.45$	(11)
Kokal and Stanislav [38]	$C_0 = 1.2$	$u_d = 0.345\sqrt{gD}\left(1-\frac{\rho_g}{\rho_l}\right)^{0.5}$	(12)
Bestion [39]	$C_0 = 1$	$u_d = 0.188\sqrt{gD}\sqrt{\frac{\rho_l}{\rho_g}-1}$	(13)
Fabre and Line [40]	$C_0 = \frac{2.27}{1+\left(\frac{Re}{1000}\right)^2} + \frac{1.2}{1+\left(\frac{1000}{Re}\right)^2}$		(14)

[1] Mostly used for bubble/slug flow patterns and often applied to small to medium pipes. [2] Equations applicable for Churn and Turbulent flows, annular flows $C_0 \to 1.0$, and drift velocity would be complex correlations often related to interfacial friction. [3] Mostly used for Churn and Turbulent flows.

2. Multiphase Flow of Liquid and Gas

Predicting flow pattern transitions is a central challenge in two-phase flow analysis. Early approaches relied on limited empirical maps, but a significant advancement was the development of mechanistic models, which predict transitions based on underlying physical principles. The model by Taitel et al. is a widely accepted example of this approach, offering greater physical insight and more reliable extrapolation compared to empirical methods [41]. The Taitel et al. map delineates flow pattern stability regions using superficial gas and liquid velocities as coordinates, modeling the physics of four key transition boundaries [41]. A major advantage of this map is its practicality. For a given set of operating conditions (e.g., pipe geometry and fluid properties), the flow pattern can be predicted using only the superficial velocities of the two phases [41].

Since the liquid phase is mostly acceptable to be considered as an incompressible flow, density can be assumed to be a constant value. However, the gas phase cannot be treated the same, as its density is highly affected by pressure variation, as shown by Equation (15), in which ψ can be calculated using Equation (16). Eventually, superficial velocities are presented in Equation (17a,b) for both phases, in which P_i is the local pressure and R_s, Z, and T are the gas-specific constant, compressibility factor, and temperature, respectively.

$$\rho_g = \frac{P_i}{\psi} \tag{15}$$

$$\psi = R_s Z T \tag{16}$$

$$u_{sl} = \frac{1}{A}\frac{\dot{m}_l}{\rho_l} \tag{17a}$$

$$u_{sg} = \frac{\dot{m}_g}{A}\frac{\psi}{P_i} \tag{17b}$$

Parameters $\dot{m}_l$ and $\dot{m}_g$ in Equations (17a,b) introduce the mass flow rate of liquid and gas phases. In a gas lift system with upward vertical flow, the behavior of each phase differs significantly, even in a simple isothermal, constant-diameter pipe. The superficial liquid velocity (u_{sl}) remains constant along the entire length of the pipe. However, the superficial gas velocity (u_{sg}) continuously increases as the fluid moves toward the outlet at the top. This is a direct result of a hydrostatic pressure drop, which reduces gas density and thus increases gas velocity to maintain a constant mass flow rate, which is a result of mass conservation. Although it may seem that the progression should appear as a horizontal trajectory on a Taitel et al. flow pattern map, this would not be a valid assumption since the flow map is constructed for a constant density of phase and since the boundaries defining the annular and slug/churn regions will be different based on densities.

2.1. Main Parameters for the Proposed Flow Pattern Map

Taitel et al.'s flow map's primary limitation is that it separates the phase velocities, failing to show their combined contribution to the total flow. The physical impact of gas dominance depends heavily on the liquid velocity (the Y-coordinate). This is reflected in the map's unbounded nature; it lacks an asymptote that would represent a physical limit on the combined mixture velocity.

The proposed flow pattern map addresses a key limitation of the original Taitel et al. map, where conditions of high mixture velocity are scattered across the plot (e.g., top left, bottom right, or top right). It simplifies this by redefining the axes.

- X-axis: Mixture Velocity (u_m)
  Instead of u_{sg}, the X-axis now represents u_m, which can be calculated using Equation (18). This provides the major benefit of consolidating all high-velocity systems to the right side of the map. It also means that the X-axis directly correlates with the system's overall volumetric flow rate.
- Y-axis: Volumetric gas quality (β_g)
  The Y-axis is changed to represent β_g. This is the ratio of the superficial gas velocity to the total mixture velocity, as mathematically represented in Equation (19). In the case of gas lift, in which mass flow rates are known instead of using superficial velocities as inputs, Equations (20) and (21) can be used to calculate u_m and β_g, respectively.

In Equations (18) and (19), Q_g, Q_m, and A are the volumetric flow rate of gas, the volumetric flow rate of the mixture, and the cross-sectional area of the pipe, respectively.

$$u_m = u_{sl} + u_{sg} = \frac{Q_m}{A} \tag{18}$$

$$\beta_g = \frac{u_{sg}}{u_m} = \frac{Q_g}{Q_m} \tag{19}$$

$$u_m = \frac{1}{A}\left(\frac{\dot{m}_l}{\rho_l} + \dot{m}_g\frac{\psi}{P}\right) \tag{20}$$

$$\beta_g = \frac{1}{1 + \frac{\dot{m}_l}{\dot{m}_g}\frac{1}{\rho_l}\frac{P}{\psi}} \tag{21}$$

This revised visualization makes it easier to identify high-flow systems immediately. It also provides a more intuitive framework for understanding how factors like drift velocity affect gas void fraction estimations within the drift–flux model. Differences in the flow pattern map axis are presented in Table 2.

Table 2. Comparison of axis values in Taitel et al. and the proposed flow map.

Axis	Taitel et al.	Proposed Flow Map
X	$u_{sg}\left(\mathrm{m.s}^{-1}\right)$	$u_m\left(\mathrm{m.s}^{-1}\right)$
Y	$u_{sl}\left(\mathrm{m.s}^{-1}\right)$	$\beta_g = u_{sl}/u_m(-)$

β_g is a dimensionless parameter that describes the gas phase's fraction of the total volumetric flow, with its value always ranging from 0 to 1. When $\beta_g \to 1$, the gas phase becomes more dominant, and $\alpha_g \to 1$. Conversely, if $\beta_g \to 0$, the liquid phase becomes the dominant phase, and $\alpha_g \to 0$. In the case of equal contribution of each phase to the total volumetric flow rate, $\beta_g \to 0.5$. In this case, the actual velocity of each phase is inversely proportional to the void fraction of the phase ($u \propto 1/\alpha$).

Rewriting DFM equations in terms of β_g shows that the value of β_g would be a function of α_g, C_0, u_d, and u_m, as represented in Equation (22).

$$\beta_g = \alpha_g\left(C_0 + \frac{u_d}{u_m}\right) \tag{22}$$

The DFM is based on drifting between phases; however, in the case of no slip, the flow profile would be flat, and there would be no drift between phases. Therefore, the values of C_0 and u_d would be 1 and 0, respectively, which will simplify the correlation to $\beta_g = \alpha_g$. However, due to the nature of these flows, since drifting would likely happen, α_g would be the lower limit for the value of β_g. This also represents a limit to α_g in the medium, too. Since gas rises faster than liquid, its void fraction will be less than the case of no slip. Thus, $\alpha_g \leq \beta_g$.

Still, further simplifications can be performed in case of the negligibility of the term u_d/u_m on higher mixture velocities. Based on most correlations represented in Table 1, drift velocity is a function of pipe diameter and fluid densities; therefore, its value would stay constant, regardless of the value of superficial velocities. In case of having higher mixture velocities, the value of drift velocity would be far less than the value of mixture velocity ($u_d/u_m \to 0$) and can be neglected for further simplifications as $\beta_g \approx \alpha_g C_0$. This simplification requires high mixture velocity, which would likely happen in annular or dispersed bubble flow patterns.

2.2. Distribution-Weighted Void Fraction

The product of α_g and C_0 can be intuitively conceptualized as the distribution-weighted void fraction (α_c) in Equation (23). While the standard void fraction simply quantifies the geometric space occupied by the gas, it fails to capture the dynamic realities of the flow. The key benefit of this weighted term is that it adjusts this simple fraction to account for how the gas is distributed across the pipe and correlated with the fluid's velocity. Consequently, it provides a more physically meaningful value that better represents the effective gas transport, leading to more accurate predictions of complex two-phase flow behavior, such as slip velocity and pressure drop. Rewriting the DFM with the integration of α_c would result in the following equations:

$$\alpha_c = \alpha_g C_0 \tag{23}$$

$$\beta_g = \alpha_c \left(1 + \frac{u_d}{C_0 u_m}\right) \tag{24}$$

2.3. Flow Pattern Transition Criteria

Taitel et al.'s flow pattern map was constructed by having different zones for each flow pattern based on the specific criteria for transitions between flow patterns [41].

2.3.1. Transition of Bubbly to Slug Flow

The shift from bubbly flow to slug flow is a critical change in two-phase dynamics where small, dispersed gas bubbles merge into large gas pockets, known as Taylor bubbles that can span the entire pipe diameter [41]. The physical mechanism driving this transition depends heavily on the liquid's flow rate. According to Taitel et al., at low liquid velocities, slug flow can exist once α_g reaches a critical value of 0.25 to 0.30. At high liquid velocities, bubbly flow may still exist at higher void fractions, but it would not be possible to have bubbly flow above α_g value of 0.52 [41]. They also believed that bubbly flow cannot exist on pipe diameters (D) smaller than a critical value presented in Equation (25) [41].

$$D = 19 \left[\frac{\sigma}{\rho_l g}\right]^{0.5} \left(1 - \frac{\rho_g}{\rho_l}\right)^{0.5} \tag{25}$$

Taitel et al. believed that the transition from bubbly flow to slug/churn can happen when u_{sg} becomes higher than a certain value in Equation (26) [41].

$$u_{sg} = \frac{1}{3} u_{sl} + \frac{1.15}{3} \left[\frac{g\sigma}{\rho_l}\right]^{0.25} \left(1 - \frac{\rho_g}{\rho_l}\right)^{0.25} \tag{26}$$

This relation can also be rewritten in terms of β_g in Equation (27). This means that if the gas volumetric quality becomes higher than a certain value, the flow would not be bubbly anymore.

$$\beta_g = 0.25 + \frac{1}{3.48} \left[\frac{g\sigma}{\rho_l}\right]^{0.25} \left(1 - \frac{\rho_g}{\rho_l}\right)^{0.25} \frac{1}{u_m} \tag{27}$$

2.3.2. Transition of Churn to Slug

As gas velocity increases beyond the stable slug flow limit, the system transitions to churn flow, a more turbulent and chaotic regime. The defining feature of churn flow is the erratic, oscillatory motion of the liquid [41]. Taitel et al. believed that the boundary of transition of churn and slug flow is a function of mixture velocity and a minimum distance from the inlet to develop stable slugs. In that case, if the point of interest is located closer to the inlet than the minimum distance required for slug formation, flow would be unstable and show churning behavior [41]. For any u_m, there is a critical distance from inlet (l_c) represented in Equation (28) in which flow is still experiencing entry turbulence and slugs cannot form [41]. Analogous to this, for any point of interest, with distance l_i from inlet, there is a maximum u_m above which stable slugs cannot exist ($u_{m,c}$) (Equation (29)) [41].

$$l_c = 40.6D \left(\frac{u_m}{\sqrt{gD}} + 0.22\right) \tag{28}$$

$$u_{m,c} = \left(\frac{1}{40.6} \frac{l_i}{D} - 0.22\right) \sqrt{gD} \tag{29}$$

Therefore, slug flow requires a specific distance from the entrance to have a chance of formation, and below that critical distance, it cannot exist ($l_i > l_c$) [41]. Analogues to this for a specific point in the pipe, mixture velocity should be less than a critical value

($u_m < u_{m,c}$); otherwise, Taylor bubbles become unstable, slugs cannot form, and churning is expected.

2.3.3. Transition to Annular Flow

At higher gas velocities, the chaotic, oscillating motion of churn flow gives way to the more structured annular flow regime. In this pattern, the gas forms a continuous, high-speed core that flows up the center of the pipe, carrying with it entrained droplets of the liquid phase, and the remaining liquid is distributed as a thin, wavy film that travels along the pipe's inner wall [41]. Taitel et al. believed that there is a critical gas core velocity below which annular flow would not be possible [41]. This phenomenon is believed to happen when u_{sg} becomes higher than critical value of Equation (30) [41].

$$u_{sg} = 3.1 \frac{\left(\sigma g(\rho_l - \rho_g)\right)^{0.25}}{{\rho_g}^{0.5}} \tag{30}$$

In terms of β_g, it can be presented by Equation (31). This means that for a specific mixture velocity, there is a lower limit of β_g above which the flow gets annular.

$$\beta_g = 3.1 \frac{(g\sigma\rho_l)^{0.25}}{{\rho_g}^{0.5}} \left(1 - \frac{\rho_g}{\rho_l}\right)^{0.25} \frac{1}{u_m} \tag{31}$$

2.3.4. Transition of Bubbly and Dispersed Bubbly Flow

In the initial stage of bubbly flow, the gas phase exists as distinct bubbles dispersed throughout a continuous liquid. As the liquid flow rate increases, liquid turbulence becomes a dominant counteracting force. This turbulence is powerful enough to shred the gas phase into smaller, more spherical bubbles [41]. This breakup mechanism actively suppresses coalescence, preventing the formation of larger slugs and creating a more stable and uniform finely dispersed bubbly flow, which depends on operating conditions and fluid properties, such as the kinematic viscosity of liquid (v_l). Transition to dispersed bubbles is expected to happen when mixture velocity becomes higher than a certain value, as presented in Equation (32) [41].

$$u_m = 4.0 \left[\frac{\sigma^{0.089}}{{\rho_l}^{0.089} {v_l}^{0.072}} g^{0.446} \left(1 - \frac{\rho_g}{\rho_l}\right)^{0.446} D^{0.429} \right] \tag{32}$$

Considering all these transitional zones, a flow map can be constructed by having the values of superficial velocities of liquid and gas and eventually distinguishing the flow pattern by knowing the position of the point of interest on the map.

2.3.5. Alternative Transition Criteria from Bubbly Flow

Integrating the DFM in the new flow pattern map gives an alternative for the criterion of transitioning from the bubble/dispersed bubble to the slug/churn region. Taitel et al.'s studies assumed that transitioning to slug will start when α_g reaches 0.25; they used correlations to estimate bubble rise velocity and drift velocity to determine the region [41]. This transition boundary can also be structured using the DFM as a criterion. Thus, instead of using bubble rise velocity and drift velocity, α_g of 0.25 can be used in the DFM. Various studies and experiments suggested that the distribution parameter in transition zone of bubble to slug is approximately 1.2 [17,18,20,21,26]. Implementing this value in Equation (22) will result in Equation (33), which represents the boundary of bubbly to the slug/churn flow pattern.

$$\beta_g = 0.25 \left(1.2 + \frac{u_d}{u_m}\right) \tag{33}$$

Their studies also mentioned the maximum α_g as 0.52 for bubbly flow at higher liquid velocities [41]. Again, this void fraction can be used in the DFM; however, several studies have shown that at high superficial mixture velocities (u_m) and when the flow is in the dispersed bubble regime, C_0 approaches unity [16]. Accordingly, by considering the general form of the DFM given in Equation (22), the transition criterion from the dispersed bubble regime to the slug/churn regime can be expressed as Equation (34).

$$\beta_g = 0.52\left(1 + \frac{u_d}{u_m}\right) \tag{34}$$

It should be noted that these zones are based on the assumptions well supported by the literature, and other flow patterns may exist in different zones in the flow map, but their presence may be unstable [41].

2.4. Transition Criteria for Gas Lift Operations

The primary goal of gas lift operations is to transport liquid from a depth to the surface by injecting gas, a process that utilizes the resulting buoyancy forces. In industrial applications, the objective is to optimize the liquid production rate for a specific, controlled gas injection rate. Under steady-state conditions, both the liquid and gas mass flow rates remain constant throughout the system [42].

While analyzing these systems, the choice of flow parameter is critical. The superficial velocity of the liquid is relatively simple to determine, as it depends primarily on its mass flow rate ($\dot{m}_l$) and the pipe diameter, assuming that the liquid is incompressible. However, calculating the gas superficial velocity is far more challenging since it is susceptible to high variations. This variability makes it an unreliable parameter when the local pressure is unknown. For this reason, the gas mass flow rate ($\dot{m}_g$) is a more robust and suitable parameter for analysis. Since it is the controlled input and remains constant under steady conditions regardless of local pressure and temperature changes, it provides a stable basis for modeling and optimization.

Using Equation (17a,b) and the transition criteria of Taitel et al. for each flow pattern, rewriting correlations in terms of pressure will result in a general form of equations, such as Equation (35) [41].

$$P_t = \psi \rho_l \frac{\dot{m}_g^{\,k_1}}{\max\left(C_F D^{k_2} + k_3 \dot{m}_l, \varepsilon\right)} \tag{35}$$

In Equation (35), P_t is the pressure in which transition can happen, and k_1, k_2, and k_3 are constants depending on the flow pattern. C_F is a function of fluid properties and flow pattern. ε is a small positive value considered to ensure non-negative values that may happen for the calculation of churning criteria at distances close to the inlet. The value of ψ will be directly correlated with temperature and compressibility of gas; in the case of considering gas as ideal, it would only be a function of temperature. Further simplification can be performed by considering the system as an isotherm with no temperature variations alongside the flow path, which will result in constant ψ. Flow patterns can be approximated by transforming the criteria used to develop flow pattern maps, and by comparing system pressure at the point of interest with these criteria, flow patterns can be found.

Table 3 presents the values of constants and parameters to be used in Equation (35) for transition criteria, which are based on the criteria introduced by Taitel et al. [41]. After calculating values for transition criteria, based on the local pressure (P_i), a comparison algorithm according to the procedure in Figure 1 can be used to categorize system flow patterns. At the first stage, based on the P_i value, it would be possible to determne whether the flow is annular or not. If not, the next stage would be to explore whether the flow

would be in the slug/churn region or the bubbly/dispersed bubble region. The next stage would be to differentiate between the latter categories.

Table 3. Parameter values for the flow transition criteria in Equation (35).

	Transition Zone	k_1	k_2	k_3	C_F
P_{t1}	Annular	2	4	0	$5.928\, g^{0.5}\, \sigma^{0.5}\, \rho_l{}^{1.5} \left[1 - \frac{P}{\psi \rho_l}\right]^{0.5}$
P_{t2}	Bubbly—Slug/Churn	1	2	0.333	$0.301\, g^{0.25}\, \sigma^{0.25}\, \rho_l{}^{0.75} \left[1 - \frac{P}{\psi \rho_l}\right]^{0.25}$
P_{t3}	Slug/Churn	1	2.5	−1	$\frac{1}{51.69}\, g^{0.5}\, \rho_l \left(\frac{l_i}{D} - 8.932\right)$
P_{t4}	Dispersed Bubbles/Bubbly	1	2.429	−1	$\pi\, g^{0.446}\, v_l{}^{-0.072}\, \sigma^{0.089}\, \rho_l{}^{0.911} \left[1 - \frac{P}{\psi \rho_l}\right]^{0.446}$

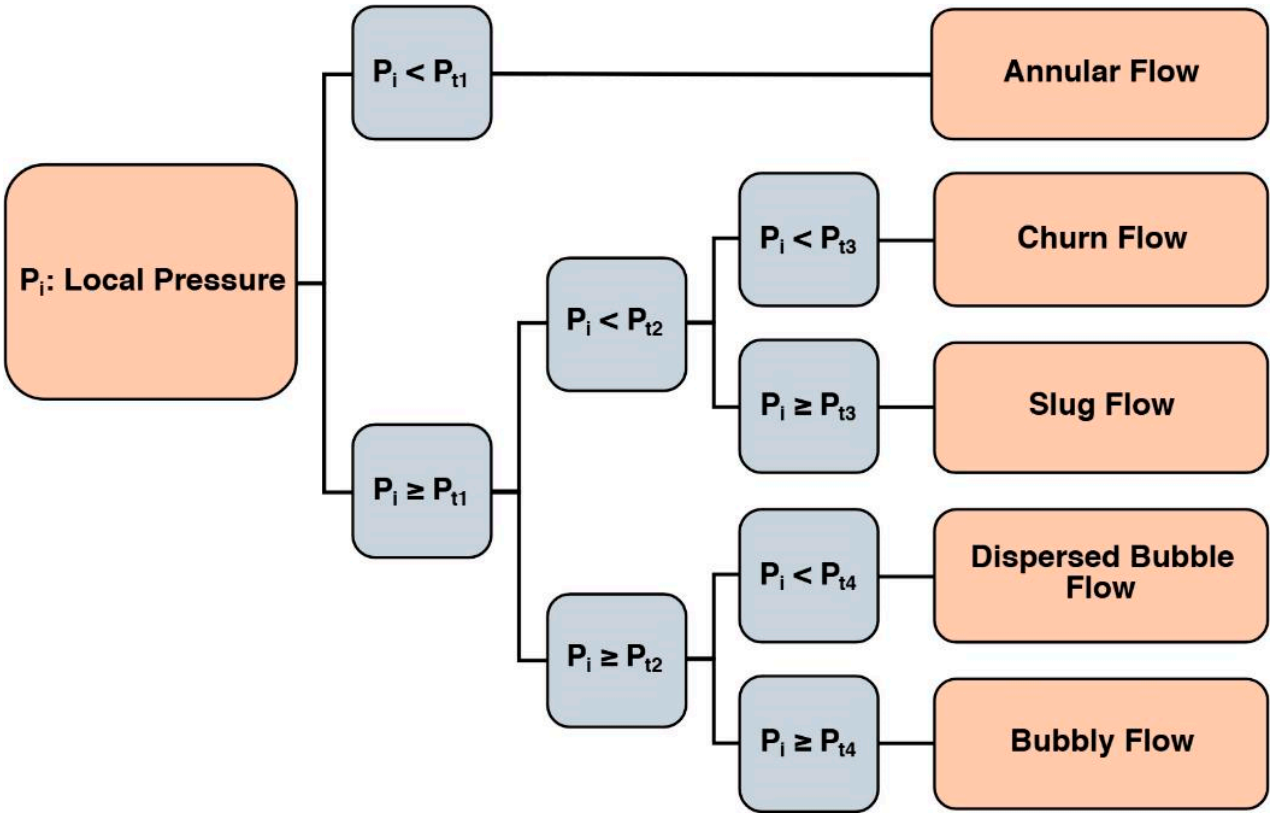


Figure 1. Flow pattern classification procedure using local pressure at the point of interest.

2.5. Drift–Flux with Pressure Approach

Following this principle, the DFM can be reformulated in terms of local pressure. This reformulation is achieved by expressing the superficial gas velocity as an explicit function of pressure. The local pressure, P_i, can be calculated using Equation (36), where parameter P_d, called drift pressure, is determined from Equation (37).

$$P_i = \left(\frac{1}{\alpha_c} - 1\right) P_d \tag{36}$$

$$P_d = \psi \rho_l \frac{\dot{m_g}^{k_1}}{C_F D^{k_2} + k_3 \dot{m}_l} \tag{37}$$

Parameters in Equation (37), which are represented in Table 4, are structurally analogous to the transition pressure criteria expressed in Equation (35). Table 4 presents a general form of the P_d equation as well as four different models for the calculation of P_d. Since DFMs are typically characterized by two key parameters of u_d and C_0, various models can be used to calculate the C_F term in P_d calculations. P_d may be simplified as a constant value in isothermal and ideal gas conditions, which makes it easier to correlate pressure at any point with α_c using Equation (36).

Table 4. Parameters used for the DFM in Equation (37).

	DFM	k_1	k_2	k_3	C_F
P_d	General	1	2	1	$\frac{\pi}{4}\frac{u_d}{C_0}\rho_l$
P_d	Nicklin et al. [26]	1	2.5	1	$0.229\, g^{0.5}\rho_l$
P_d	Zuber and Findlay [14]	1	2	1	$g^{0.25}\sigma^{0.25}\left(1-\frac{P}{\psi\rho_l}\right)^{0.25}\rho_l$
P_d	Greskovich and Cooper [34]	1	2.5	1	$0.527\, g^{0.5}\rho_l$
P_d	Kokal and Stanislav [38]	1	2.5	1	$0.226\, g^{0.5}\left(1-\frac{P}{\psi\rho_l}\right)^{0.5}\rho_l$

3. Development of a Flow Pattern Map

3.1. Proposed Flow Pattern Map

The proposed flow pattern map was constructed based on the criteria that Taitel et al.'s map was built on and the DFM formulation [14,41]. Figures 2 and 3 are samples of original and proposed flow pattern maps for a case of a 5.074 cm diameter pipe in the same operational condition. Curvatures for the transition of slug and churn are a function of entrance length. Therefore, similar to the original approach, a set of curvatures is presented in both figures for various ratios of critical distance from the entrance to the diameter.

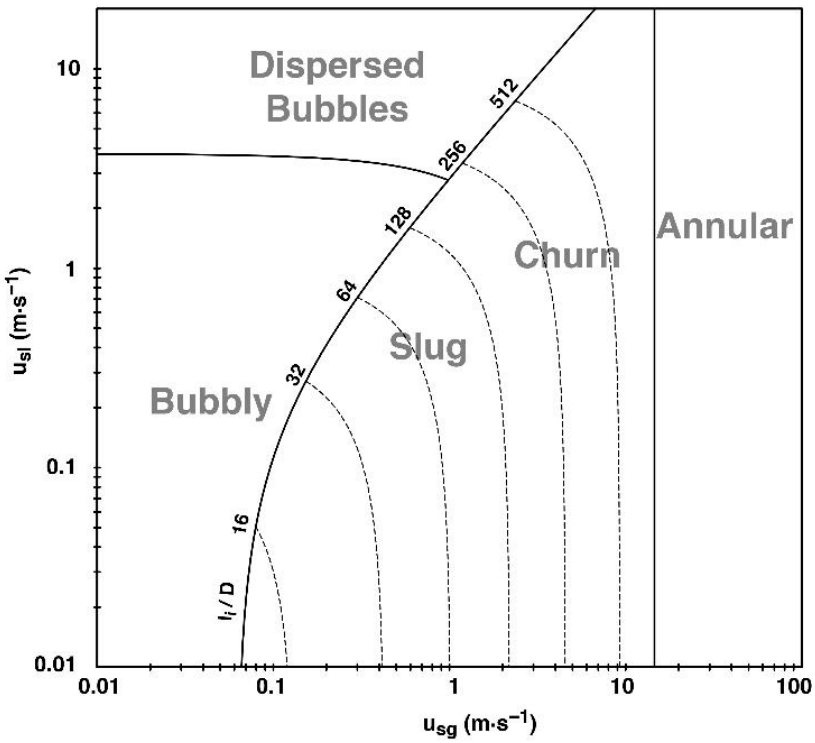


Figure 2. Taitel et al.'s flow pattern map constructed for D = 5.074 cm, T = 293.15 K, and P = 1 atm.

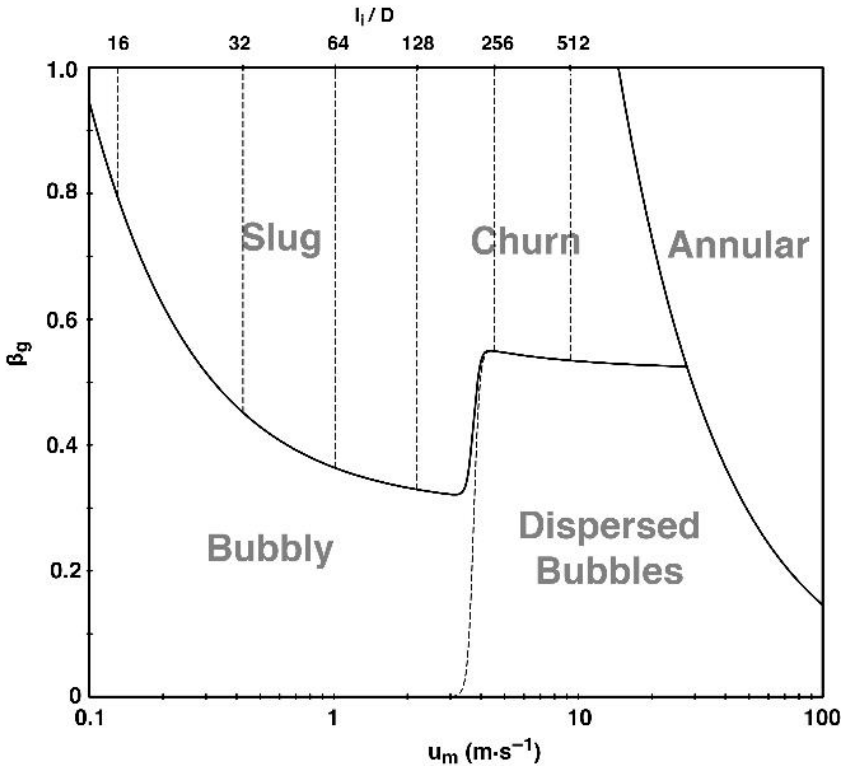


Figure 3. Proposed flow pattern map constructed for D = 5.074 cm, T = 293.15 K, and P = 1 atm.

The transition of the churn to slug flow pattern is better visualized in Figure 4 for a pipe with a diameter of 5 cm. Based on the criteria of Equations (28) and (29), transition to slug flow requires moving 0.74, 3.35, and 29.43 m from the entrance when the mixture velocity is 0.1, 1, and 10 m/s, respectively. In other words, in the case of having a higher volumetric flow rate of the mixture, the system needs more distance in the pipe to have stable slug flow. This also makes it easier to estimate the flow pattern based on the mixture velocity; for instance, if the mixture velocity becomes over 3.3 m/s in a pipe with 10 m length (in this case of study), slug flow will not form anywhere in the pipe since the entrance length required for the development of slug bubbles would be higher than the pipe's length.

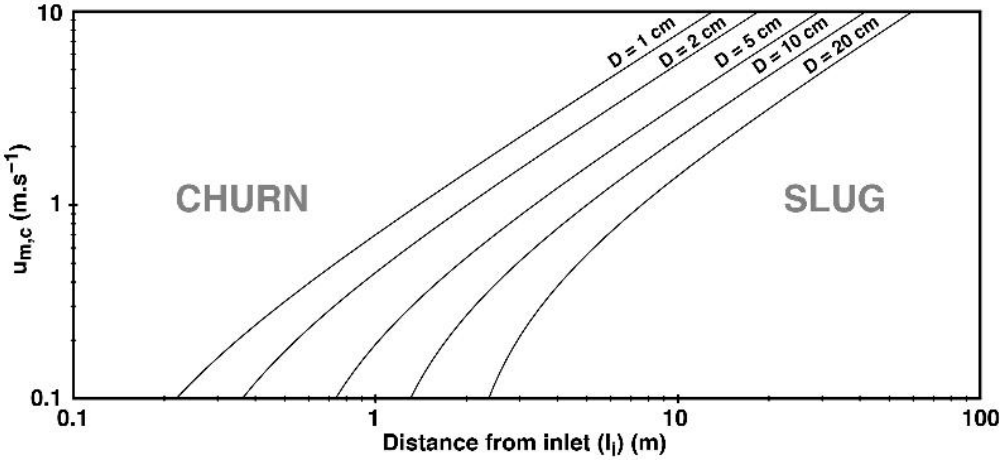


Figure 4. Sample of critical mixture velocity of slug/churn flow patterns relative to the distance from the inlet.

It should be noted that since these flow patterns are developed for a specific point of interest in the pipe, they may not be applicable to all points on longer pipes; however, if the

pressure difference from the inlet to outlet is not high enough to cause a high variation of gas density, a specific flow map developed for a certain point of interest may still be able to predict the transition of bubbly to slug/churn flow patterns and the transition boundary of slug and churn flow in other points. However, it is not accurate for predicting the transition to annular flow, as it is highly sensitive to gas density, and its applicability is limited when variations in gas density are neglected.

Like the original flow pattern developed by Taitel et al., superficial velocities of phases can be presented on the flow pattern, as depicted in Figure 5. The addition of these curvatures also presents the possibility and impossibility of a certain flow pattern at certain superficial velocities of each phase. Additionally, in the case of a constant diameter of flow and steady state, since the superficial velocity of liquid stays constant in upward flow, each curvature specific to a certain superficial velocity of liquid can present the path of flow when the mixture ascends toward the surface. However, as mentioned before, the estimation of the flow pattern should be used with caution since the flow pattern map is specific to certain operating conditions of flow, and boundaries of transitioning zones shift because of parameter variation.

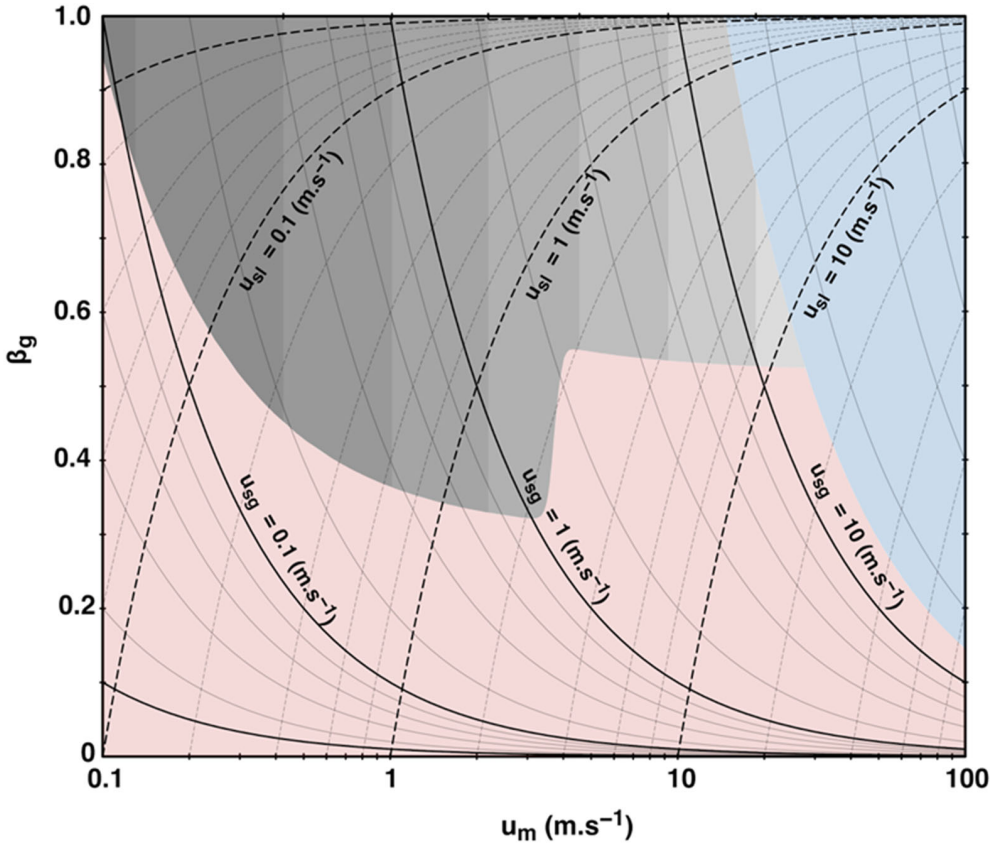


Figure 5. Curvatures of superficial velocities of phases on the flow pattern map for D = 5.074 cm.

3.2. Estimation of the Gas Void Fraction

Another shortcoming of traditional maps is their inability to provide an estimate for the gas void fraction. This new approach overcomes that limitation by directly integrating the DFM into the map's framework. As a result, the map can provide the value of α_c for any point. Having this value makes it possible to have an estimation of the void fraction by knowing the distribution parameter. Many existing models simplify this by treating C_0 as a constant or as a simple function of fluid densities. However, experimental data from the literature show that C_0 can vary between different flow patterns or different values of void fractions in the system, especially when a constant drift velocity is assumed. This suggests

that an accurate estimation of the void fraction requires a model where C_0 is not a universal constant but is instead dependent on flow conditions, such as the void fraction of gas or turbulence of the flow [16,20,36,40].

Using different values of α_c in Equation (24), Figure 6 can be constructed, which shows the curvatures of void fraction estimators on top of the proposed flow pattern map. Since the term C_0 appears in the dominator of Equation (24), an estimate of C_0 is required in order to construct the corresponding curves. In lower void mixture velocities, a value of 1.2 seems reasonable based on various studies [14,26,33,38]. However, this value can be reduced to a value of 1.0 when reaching higher mixture velocities [16]. It should be noted that in higher mixture velocities, curvatures are not highly sensitive to variations of u_m for assumed values of C_0. To better explain this, the partial derivative of β_g relative to u_m based on the DFM will result in Equation (38).

$$\frac{\partial \beta_g}{\partial u_m} = -\alpha_g u_d \frac{1}{{u_m}^2} \tag{38}$$

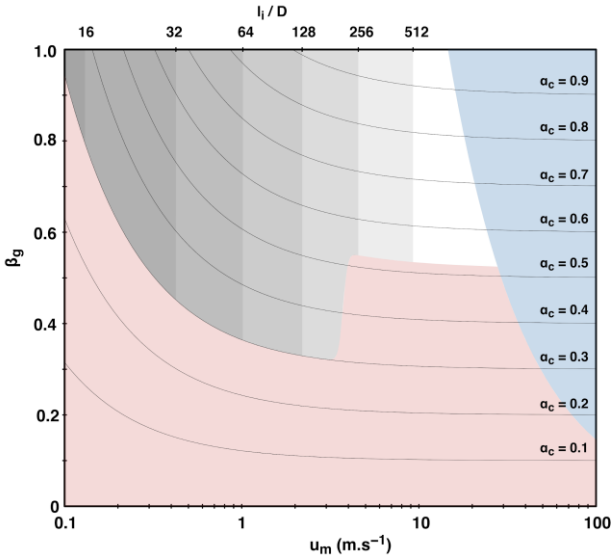


Figure 6. Addition of distribution-weighted void fractions to the flow pattern map (D = 5.074 cm, T = 293.15 K, P = 1 atm).

This presents the lower effect of the drift velocity on higher mixture velocities ($u_d \ll u_m$). For instance, the value of u_d for a pipe with a diameter of 5.074 cm is approximately 0.24 m/s (according to Nicklin et al.'s model), and multiplying the void fraction will make its value even smaller. Considering this, as an example, at a mixture velocity of 4.9 m/s, the drift velocity will affect the result by less than 1%.

3.3. Classification of Flow Patterns in Gas Lift Scenarios

To elucidate the dependence of transition pressure criteria on phase mass flow rates, Figures 7 and 8 were generated for a two-phase system comprising air and water at a temperature of 293.15 K within a 10 cm diameter pipe. Figure 7 illustrates the influence of varying $\dot{m}_l$ on transition boundaries at fixed $\dot{m}_g$ values of 0.05, 0.15, and 0.25 kg/s. It is observed that increasing the gas injection rate expands the possibility domain of the annular flow pattern at a given pressure since it increases the superficial velocity of gas. Consequently, for a steady-state vertical flow, the operational pressure profile of the pipe corresponds to a vertical line on this map. Furthermore, the demarcation of the slug/churn region is shown to be a function of the hydrodynamic entrance length, with fully developed slug flow being more probable at greater distances from the inlet.

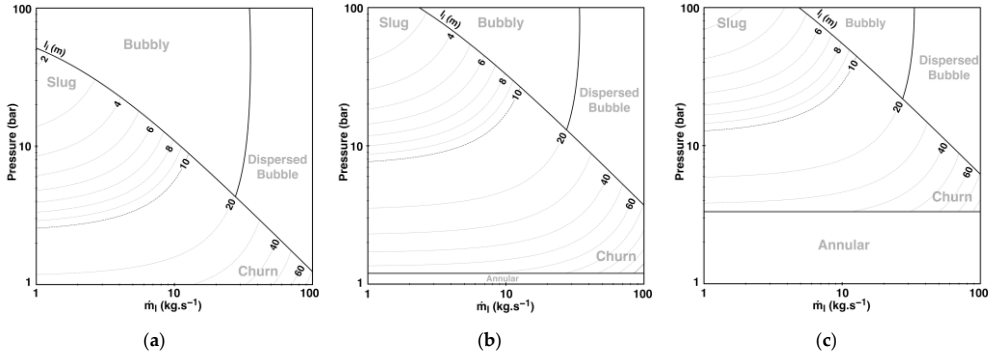


Figure 7. Transition pressure vs. mass flow rate of the liquid phase (D = 10 cm): (**a**) gas injection rate of 0.05 kg/s; (**b**) gas injection rate of 0.15 kg/s; and (**c**) gas injection rate of 0.25 kg/s.

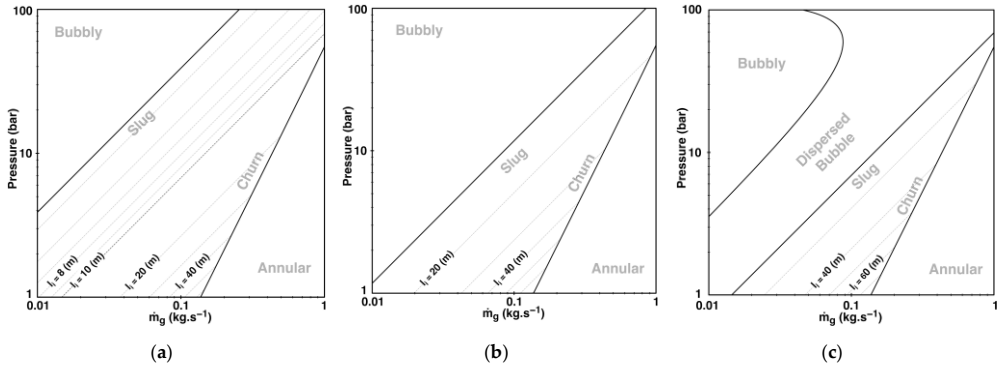


Figure 8. Transition pressure vs. injection rate of the gas phase (D = 10 cm): (**a**) liquid mass flow rate of 15 kg/s; (**b**) liquid mass flow rate of 25 kg/s; and (**c**) liquid mass flow rate of 35 kg/s.

Figure 8 provides a complementary analysis, illustrating the effect of varying $\dot{m}_g$ for systems with a fixed liquid throughput. This representation is instructive for design cases where a specific liquid production rate is the primary objective. These maps demonstrate that a higher $\dot{m}_l$ contracts the slug/churn transition window while expanding the stability regions for both dispersed bubble flows at higher pressures and annular flows.

Furthermore, a critical value of $\dot{m}_l$ as a threshold for the existence of the dispersed bubble regime is identified. Based on the Taitel et al. criteria applied to this system, a dispersed bubble flow cannot be sustained at $\dot{m}_l$ below approximately 27 kg/s for pressures of up to 100 bar (for this specific case). This phenomenon explains the observed flow maps in Figure 8. The dispersed bubble regime is absent in Figure 8a,b, where $\dot{m}_l$ is below this critical value, but it is present in Figure 8c, where it exceeds the threshold.

Transition between slug and churn depends on the distance from the inlet; therefore, several curvatures are presented to help identify the flow pattern in the slug/churn window in Figures 7 and 8.

For a steady-state flow in an isothermal, constant-diameter pipe with an incompressible liquid phase ($u_{sl} = constant$), the variation of u_m is solely a function of u_{sg} variations. Given the inverse relationship between u_{sg} and local pressure due to gas compressibility, a higher u_m corresponds to a lower local pressure. This relationship implies that for flow patterns other than the annular or bubbly flow, the local pressure should exceed a critical threshold (P_{t3}) to sustain stable Taylor bubbles. If the pressure falls below this threshold, the flow transitions to the churning zone.

3.4. Flow Pattern Classification for the Experimental Results

The vertical pressure isopleths on the previously discussed flow (Figures 7 and 8) can be coupled with a hydrodynamic pressure gradient model to predict the evolution of the

flow pattern as a function of vertical pipe depth. To illustrate this methodology, a case study based on the experimental work of Saito et al. was numerically modeled, with the results presented in Figure 9a [43]. This case study is based on a 196.6 m vertical pipe with a 15.1 cm diameter, transporting water at 77.96 kg/s via an injected air mass flow rate of 0.51 kg/s.

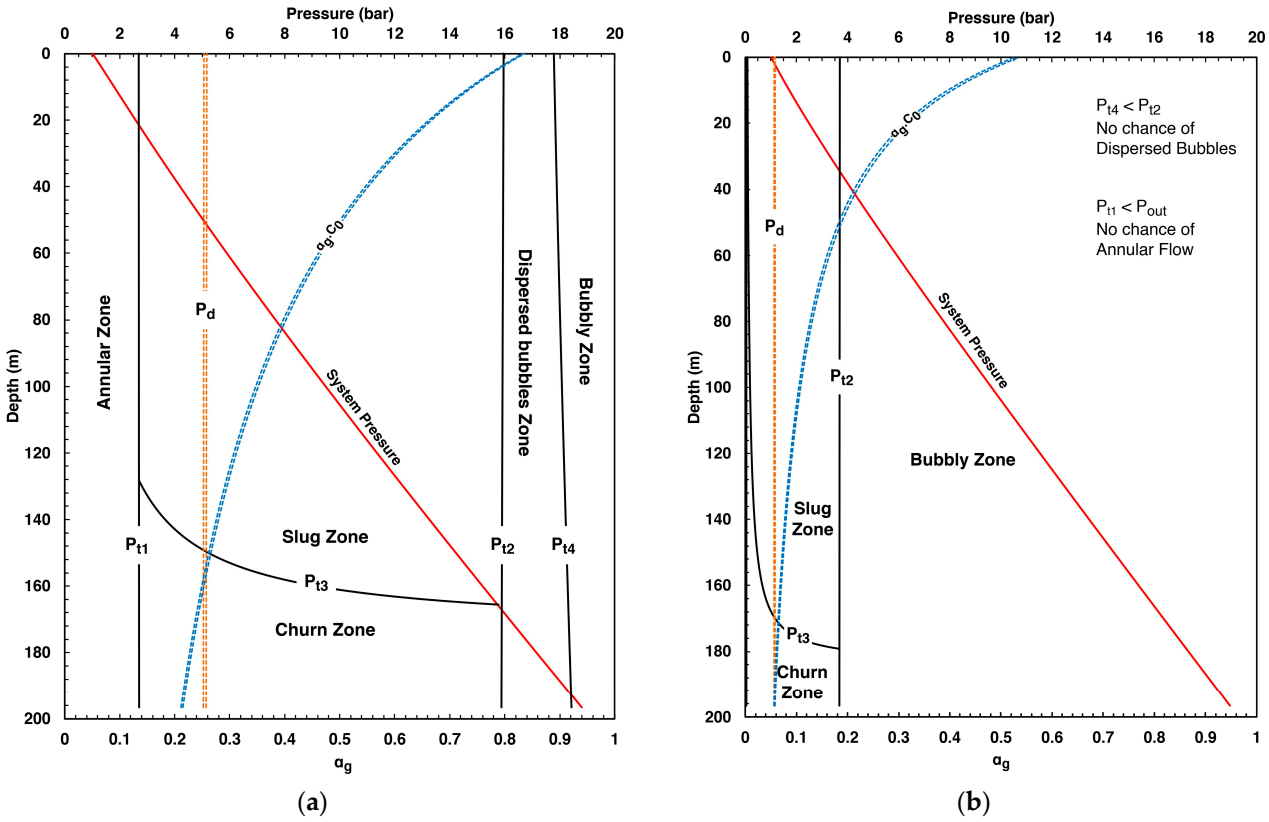


Figure 9. Pressure profile and transition criteria for a case study based on a numerical simulation of the experiments of Saito et al.: (**a**) gas injection rate of 0.51 kg/s and liquid mass flow rate of 77.96 kg/s; (**b**) gas injection rate of 0.066 kg/s and liquid mass flow rate of 41.95 kg/s.

In this case, the simulation predicts an initial bubbly flow pattern near the inlet, which transitions to dispersed bubble flow as the pressure drops below the P_{t4} threshold. As the fluid ascends further, the pressure falls below P_{t2}, precluding the existence of a stable bubbly flow and causing a transition into the slug/churn zone. Initially, the flow exhibits churning characteristics as the entrance length is insufficient to satisfy the slug formation criterion ($P < P_{t3}$). By ascending further, this criterion is met ($P > P_{t3}$), and the flow stabilizes into the slug regime. This pattern persists until reaching a depth of 22.35 m, at which point the pressure drops below P_{t1}, and the flow turns to an annular pattern for the remainder of its ascent to the surface. It should be noted that the reference point for the calculation of depth is considered as the outlet of the pipe, which is located 12.6 m above sea level.

It is important to clarify that although mixture velocity increases when moving upward, it does not mean that the flow will have a higher chance of churning, even though churning requires higher mixture velocity when studying a specific point of interest. For example, at a depth of 160 m in the case study, the transition criteria are calculated as $P_{t1} = 2.7\ bar$, $P_{t2} = 15.89\ bar$, $P_{t3} = 9.14\ bar$, and $P_{t4} = 18.29\ bar$, while the local system pressure is $P_i = 15.19\ bar$. Following the determination algorithm in Figure 1, since $P_i > P_{t1}$ and $P_i < P_{t2}$, the flow is neither annular nor bubbly. Since $P_i > P_{t3}$, the conditions for a stable slug flow are met. However, if the mixture velocity at this location was higher,

the corresponding local pressure (P_i) would be lower, approaching the P_{t3} threshold and thereby increasing the propensity for the flow to transition into the churn flow pattern.

A second operating scenario from the same experimental series was simulated for comparison, with the results shown in Figure 9b. In this simulation, the gas injection rate was significantly lower at 0.066 kg/s, lifting a liquid rate of 41.95 kg/s. While the pipe dimensions and bottom-hole pressures were the same, the primary distinction is the resulting superficial velocity ranges. For the first case, u_{sl} was 4.36 m/s and u_{sg} had a range of 1.28 to 23.89 m/s. For the second case, superficial velocities were lower, and u_{sl} was 2.35 m/s, while u_{sg} ranged from 0.16 to 3.09 m/s. This substantial reduction in phase superficial velocities is the reason that the flow in the second case was predominantly within the bubbly flow zone.

The profiles of P_d and $\alpha_g C_0$ for two case studies are presented in Figure 9 as bands rather than single curves because the term C_F in Table 4 used in calculation is itself a function of C_0. These bands represent the variation resulting from assuming that C_0 ranges from 1.0 to 1.3 within the C_F parameter. The narrowness of these bands suggests that the sensitivity of C_F to the assumed value of C_0 is not significant, particularly at higher volumetric flow rates, according to Equation (24) ($u_d \ll C_0 u_m$). However, in stark contrast, the final estimation of the void fraction α_g from the value of α_c remains sensitive to the chosen value of C_0. Therefore, for computational convenience and improved clarity, it can be advantageous to treat these two values of C_0 separately.

4. Development of a Model for Gas Void Fraction Estimation

4.1. Estimation of a Distribution Parameter

In case of having the proper model for u_d, at any point on the flow pattern map, the distribution parameter (C_0) can be calculated using Equation (39), which is based on the reformulation of the DFM.

$$C_0 = \frac{\beta_g}{\alpha_g} - \frac{u_d}{u_m} \tag{39}$$

Numerous correlations for the estimation of C_0 and u_d have been proposed within the framework of the DFM. The work of Shi et al. on large diameter pipes, for instance, demonstrates that these parameters are not constant but exhibit a strong dependence on the gas void fraction [44]. They reported that C_0, typically valued at approximately 1.2 in the bubbly flow, decreases as α_g increases. This decrement accelerates as α_g approaches its high limit of 1.0, presenting pure gas flow. Furthermore, Shi et al. describe a non-monotonic behavior for u_d as a function of α_g. The drift velocity is initially low at small void fractions within the bubbly zone, then increases rapidly to a peak value at an intermediate void fractions, and subsequently decreases, approaching zero as the flow becomes entirely gaseous ($\alpha_g \to 1$) [44]. Their model, therefore, predicts u_d values which are initially lower than those proposed by simpler correlations; however it may surpass the predictions of those models in the intermediate void fraction range.

Contrary to the values predicted for the turbulent flow, several studies have reported significantly higher distribution parameters in the laminar flow regime of the liquid phase [40,45,46]. The experiments by Fréchou demonstrated that for Reynolds numbers below 500, C_0 approaches a value of 2.3 [45]. Numerical simulations by Zai-Sha Mao and Dukler corroborate these findings [46]. Similarly, a comprehensive study conducted by Fabre and Line found that C_0 could reach values as high as 2.27 within the laminar zone [40].

4.1.1. Chexal et al.'s Model

One of the more comprehensive models for the estimation of C_0 is the model offered by Chexal et al., which is presented in Equation (40a–g) [47].

$$Re = \max\left(Re_l, Re_g\right) \tag{40a}$$

$$A_1 = \frac{1}{1 + e^{-\left(\frac{Re}{60000}\right)}} \tag{40b}$$

$$B_1 = \min(0.8, A_1) \tag{40c}$$

$$r = \frac{1 + 1.57\frac{\rho_g}{\rho_l}}{1 - B_1} \tag{40d}$$

$$K_0 = B_1 + (1 - B_1)\left(\frac{\rho_g}{\rho_l}\right)^{\frac{1}{4}} \tag{40e}$$

$$L = \min\left(1.15{\alpha_g}^{0.45}, 1\right) \tag{40f}$$

$$C_0 = \frac{L}{K_0 + (1 - K_0){\alpha_g}^r} \tag{40g}$$

Chexal et al.'s model captures the effects of turbulence and void fraction in its formulation [47]. However, the model incorporates limiting functions to constrain its parameters. For instance, the B_1 term becomes constant for Reynolds numbers exceeding a threshold value 83,178. Similarly, the parameter L reaches a constant value for void fractions greater than 0.733 [47].

By expressing the superficial phase velocities in terms of β_g, the Reynolds numbers for the liquid and gas phases (Re_l, Re_g) can be formulated as shown in Equation (41a,b), in which μ_l and μ_g denote the dynamic viscosities of the liquid and gas phases, respectively.

$$Re_l = \frac{\rho_l}{\mu_l}(1 - \beta_g)u_m D \tag{41a}$$

$$Re_g = \frac{\rho_g}{\mu_g}\beta_g u_m D \tag{41b}$$

The determination of the maximum phase Reynolds number, a required input for Chexal et al.'s model, is independent of the mixture velocity and pipe diameter, depending only on the fluid properties and β_g, and it can be calculated using Equations (42) and (43). β_t represents the point at which gas turbulence becomes higher than that of the liquid's ($Re_g > Re_l$).

$$\beta_t = \frac{1}{\frac{\rho_g}{\rho_l}\frac{\mu_l}{\mu_g} + 1} \tag{42}$$

$$Re_{max} = \begin{cases} Re_l, & \beta_g \leq \beta_t \\ Re_g, & \beta_g > \beta_t \end{cases} \tag{43}$$

According to the Chexal et al. model, C_0 exhibits a non-monotonic dependence on the gas void fraction [47]. Initially, C_0 increases with increasing α_g; however, at α_g of approximately 0.733, the trend reverses, and C_0 subsequently decreases, approaching a value of 1.0 as $\alpha_g \to 1$. In contrast, α_c increases monotonically from 0 to 1 across the entire void fraction range, with its inflection point located at $\alpha_g = 0.733$. This implies that in the high void fraction region, the decrease in C_0 is inversely correlated to the increase in α_g.

4.1.2. Effects of Chexal et al.'s Parameters on the Distribution-Weighted Void Fraction

Combining the concept of α_c and C_0 calculated using the Chexal et al. model, the parameter α_c can be expressed as follows [47]:

$$\alpha_c = \frac{\alpha_g L}{K_0 + (1 - K_0)\alpha_g{}^r} \tag{44}$$

Their model predicts that the peak value of C_0 based on the value of α_g is influenced by fluid properties and flow dynamics. The maximum peak value is attained under conditions of lower gas density and lower turbulence (low Reynolds number), and the minimum peak value occurs with denser gas and a fully turbulent flow [47]. The distribution parameter is generally higher when there is a large density contrast between the phases and when the flow is less turbulent, a condition associated with a non-uniform velocity profile.

Figure 10 illustrates the value of α_c at maximum C_0 predicted using Chexal et al.'s model [47]. It is found that higher turbulence shifts the location of the maximum C_0 to a lower α_c value, whereas a decrease in gas density shifts it to a higher α_c value. In processes such as gas lift, where higher gas void fractions are strongly correlated with lower gas densities due to pressure drop, the peak of the distribution parameter is expected to occur in the range of $\alpha_c = 0.85 \pm 0.05$.

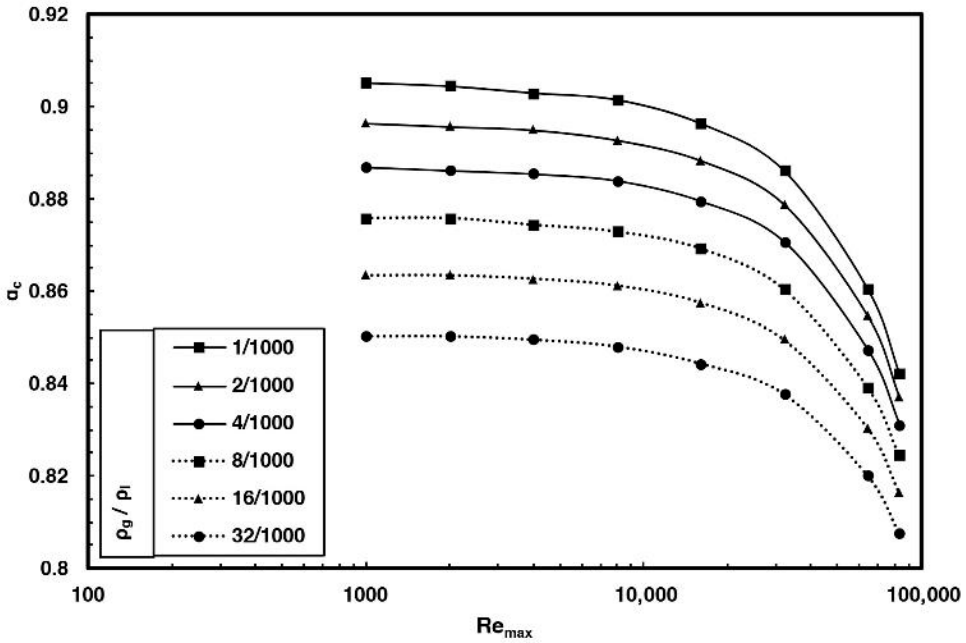


Figure 10. Value of maximum α_c when C_0 reaches its maximum value based on the Chexal et al. model vs. the maximum Reynolds number.

These concepts can also be presented in terms of the relation between the pressure and the maximum distribution parameter using Equation (36). This is advantageous for systems like gas lift, where calculating the local pressure is more straightforward than determining local superficial velocities. According to this criterion, C_0 attains its maximum at a specific pressure point; at pressures below this value, C_0 subsequently decreases. Visualization of this concept can be seen in Figure 11.

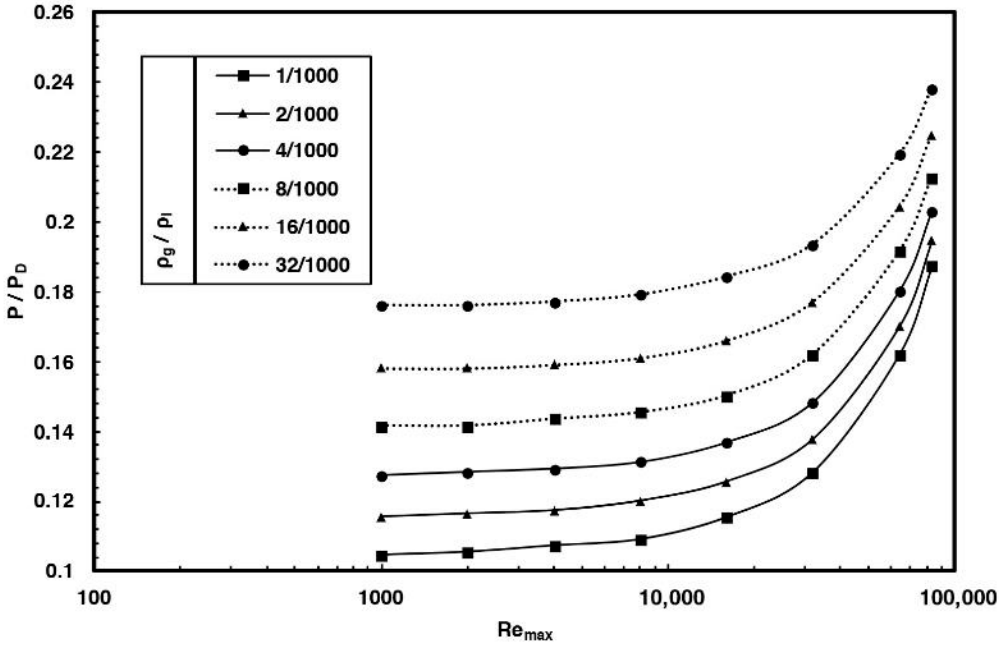


Figure 11. Pressure criteria in which C_0 reaches its maximum value based on the Chexal et al. model vs. the maximum Reynolds number.

For a gas lift operation in which mass flow rates are known, the Reynolds number of each phase can be calculated using Equation (45).

$$Re = \frac{4}{\pi} \frac{\dot{m}}{\mu D} \tag{45}$$

Given that the gas mass injection rate is a known and is a constant parameter, the gas phase Reynolds number remains constant throughout the pipeline. The liquid phase Reynolds number also becomes constant upon reaching steady state.

4.2. Analysis of Distribution Parameter Values

Using approximately 400 data points from experiments from small- to large-diameter pipes (1.27 cm to 15 cm) and using air as the gas phase and water as the liquid phase, a set of analyses was performed to observe the shortcomings of the current models, observe C_0 values, and verify the proposed model [3,48–51].

To investigate the effects of the flow condition on C_0, experimental data from Fernandes and Godbole et al. were used to determine the corresponding C_0 for each data point [3,48]. To visualize the results, points corresponding to high-distribution parameter values ($C_0 > 1.2$) and low-distribution values ($C_0 < 1.1$) were plotted on the proposed flow pattern map, presented as Figure 12. For comparison with the Chexal et al. model, contours of the constant maximum phase Reynolds number were superimposed on the map [47].

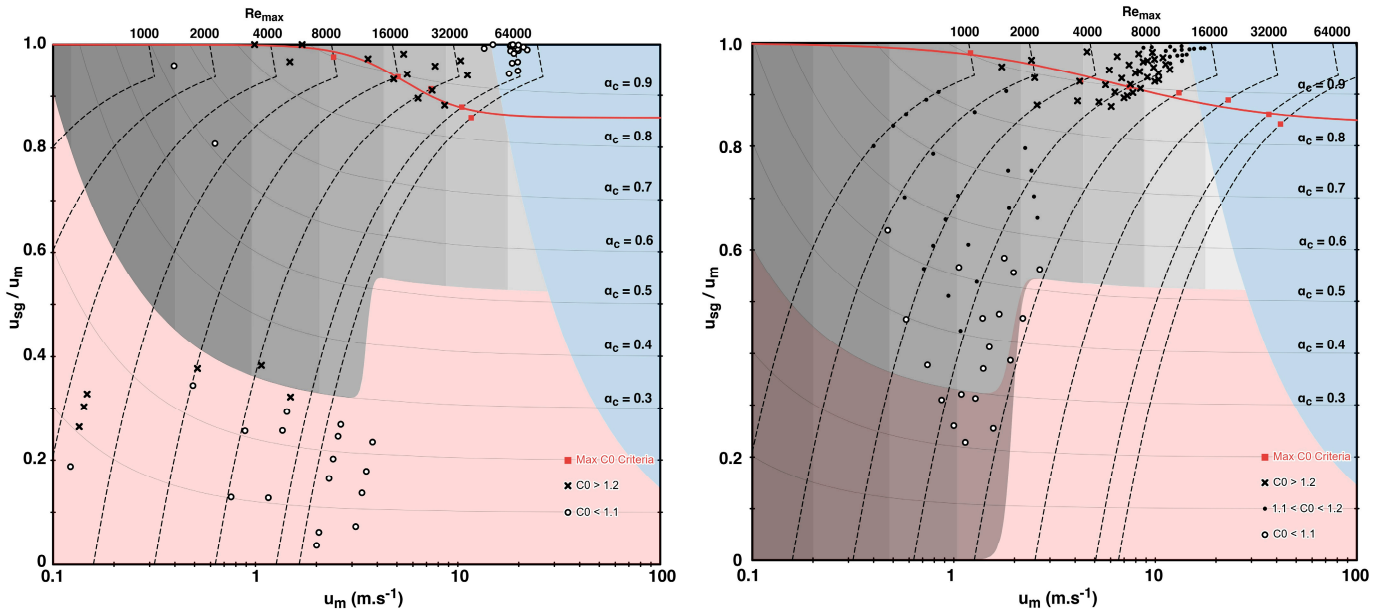


Figure 12. Distribution of experiments with the highest and lowest observed value of C_0 and comparison with the Chexal et al. criteria: (**a**) D = 5.074 cm; (**b**) D = 1.027 cm.

The locus of the maximum C_0, as predicted by the Chexal et al. criteria, is also plotted on Figure 12 [47]. As is observed, the experimental data exhibit a strong spatial correlation with the model's prediction. Experimentally determined high C_0 values cluster near the predicted contour. Conversely, data points situated far from this contour, particularly those in the annular and dispersed bubble regimes, correspond to the lowest values of C_0. While most data points conform to this trend, some outliers are observed in transitional regions, such as the onset of the bubbly flow (characterized by low gas Reynolds numbers) and the bubbly-to-slug transition.

A key finding is that an increase in mixture velocity shifts the locus of the maximum C_0 value to lower α_c values, which are consistent with observations in Figure 10. At low mixture velocities, the maximum C_0 is expected to occur at α_c values approaching 0.9, whereas at higher velocities, these peaks shift to lower α_c values before stabilizing. A parallel trend is observed with β_g, where the value corresponding to the maximum C_0 decreases from nearly $\beta_g \approx 1$ at lower mixture velocities to approximately $\beta_g \approx 0.85$ at higher velocities.

Although the Chexal et al. model provides a robust estimation for the locus of the maximum C_0, the exact value may require further analysis, as the flow map is dependent on local operating conditions. Nevertheless, the delineation of this "maximum C_0 contour" on the flow map provides a simplified, semi-empirical methodology for approximating the void fraction. By determining a point's proximity to this contour on the map, one can estimate whether the local distribution parameter is high (close to the contour) or low (far from the contour), thereby improving the accuracy of void fraction calculations from superficial velocity inputs.

Studies by Godbole et al. identified the model proposed by Nicklin et al. (Equation (4)) as a robust formulation across a wide range of void fractions [3]. This model employs a constant distribution parameter of $C_0 = 1.2$ and utilizes a drift velocity correlation analogous to that proposed by Kokal and Stanislav at low gas densities (Equation (12)) [26, 38]. Adopting this conventional drift velocity model, C_0 is calculated for two experimental datasets. As shown in Figure 13, a comparison is made against the values predicted by

the Chexal et al. model. The results indicate that the Chexal et al. model underpredicts the distribution parameter at low void fractions ($\alpha_g < 0.5$) relative to the experimentally derived values. This discrepancy does not necessarily invalidate the Chexal et al. model, as the drift–flux parameters (C_0 and u_d) are inherently coupled. The Chexal et al. distribution parameter is intended for use with its own corresponding, and more complex, drift velocity model [47]. Therefore, if a conventional drift velocity correlation is employed, it may be necessary to impose a lower bound on the distribution parameter predicted by the Chexal et al. model. A further challenge associated with the application of the Chexal et al. model is its computational complexity; the dependence of the distribution parameter on the void fraction necessitates an iterative solution procedure.

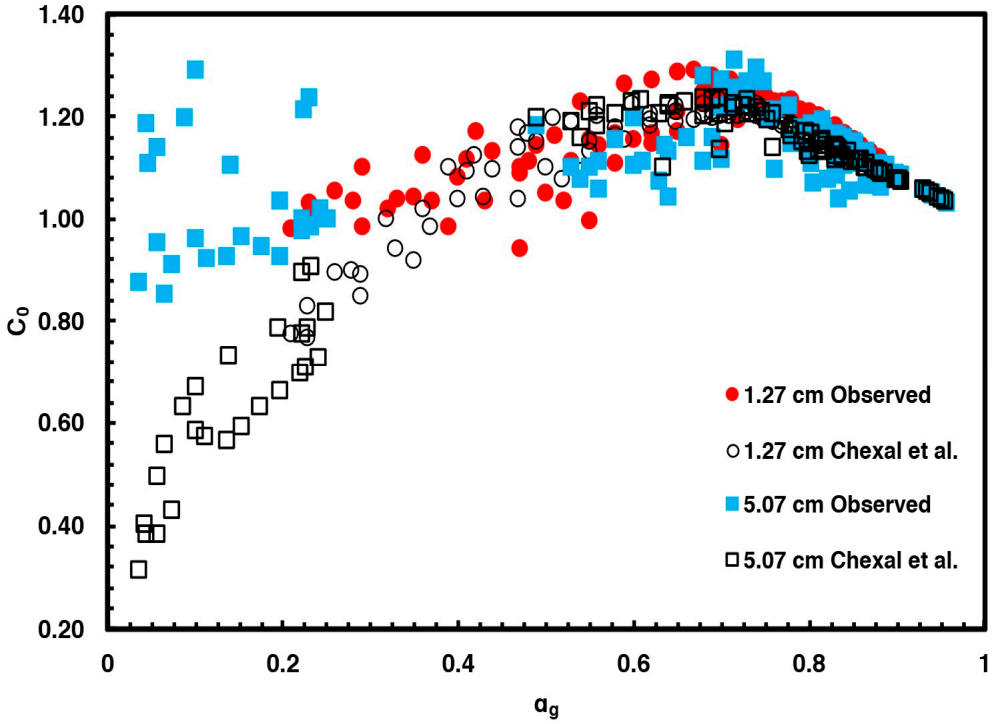


Figure 13. Comparison of C_0 calculated using the Chexal et al. model and experimental observations.

4.3. Proposed Model for Estimation of the Gas Void Fraction

In the proposed model, the distribution parameter is formulated as a function of the product of α_g and C_0 itself to reflect physical flow structure changes. As the flow evolves from dispersed bubbles to Taylor bubbles, gas concentrates in the high-velocity core, driving C_0 to a peak. Conversely, the transition to annular flow creates a continuous gas core that uniformizes the velocity profile, forcing C_0 back towards 1 [44,47]. Consequently, the inflection point of α_c serves as a quantitative marker for this physical shift from slug/churn dominance (high C_0 values) to annular dominance. This product, termed the distribution-weighted void fraction, α_c, calculated using Equation (23), serves as an effective void fraction that governs the flow dynamics. Based on the empirical evidence presented in Figure 12, the model shows that C_0 attains its maximum value at around $\alpha_c \approx 0.9$. In case of plotting α_c against C_0, a value of $\alpha_c \approx 0.9$ will be the inflection point of the curvature. As this product approaches its upper limit of unity, C_0 must also approach 1. This behavior is consistent with the physical constraint that as $\alpha_g \to 1$, C_0 should also approach 1, and it is in agreement with the trends predicted by the Chexal et al. model, the findings of Shi et al., and the trend observed in Figure 13 [44,47]. At lower values of α_c, the behavior of C_0 is more complex and regime-dependent. Specifically, for flow system in the laminar

regime, C_0 can attain significantly higher values ($C_0 > 1.2$), whereas for the dispersed bubble regime, it approaches a value of 1.0.

The proposed model is based on two ranges for values from 0 to the inflection point of α_c and values above the inflection point to 1. This model is presented as a combination of a logistic function and an exponential function, and C_0, can be calculated as a function of α_c using Equations (46)–(48) as follows:

$$\alpha_c = \frac{\beta_g}{1 + \frac{u_d}{C_{0A} u_m}} \tag{46}$$

$$C_{0L} = C_{0MIN} + (C_{0MAX} - C_{0MIN}) \left(\frac{1}{1 + e^{\lambda_1 (\alpha_{c0} - \alpha_c)}} \right) \tag{47a}$$

$$C_{0H} = 1 + (C_{0MAX} - 1) \left(1 - e^{\lambda_2 (1 - \alpha_c)} \right) \tag{47b}$$

$$C_0 = \min(C_{0L}, C_{0H}) \tag{47c}$$

$$\alpha_g = \frac{\alpha_c}{C_0} \tag{48}$$

This model relies on sets of parameters and coefficients. C_{0L} and C_{0H} represent the lower range and the higher range of C_0 correlations for values of α_c that are less than and more than the inflection point, respectively. C_{0MAX} and C_{0MIN} define the maximum and minimum asymptotic values of C_0. The coefficient λ_1 controls the initial gradient of C_0 as α_c increases, while the descending behavior of the function is governed by λ_2, which determines the rate of at which C_0 decays as α_c approaches unity. A value of α_{c0} represents the average value of α_c at the point of transition from the bubbly flow and the value of α_c at which the C_0 is the highest. Through calibration against the experimental data, optimal values for these parameters were established. A robust fit was achieved using $C_{0MAX} = 1.23$, $C_{0MIN} = 1.05$, $\lambda_1 = 8$, $\lambda_2 = -32$, and $\alpha_{c0} = 0.6$, as these values provided satisfactory results and were employed in all model computations.

The nature of these calculations requires iterations since C_0 is used for the initial stage of calculations in Equation (46), as C_{0A}, which is again calculated in Equation (47c); however, the parameter C_{0A} can be approximated as a constant value of 1.2, as its influence on system dynamics diminishes at higher mixture velocities ($u_d \ll C_0 u_m$). Therefore, neglecting its predicted decline under these conditions introduces negligible error. For gas lift operations, a specific formulation for α_c, Equation (49), can be used for calculation instead of using Equation (46). Equation (49) utilizes local pressure and drift pressure as an alternative to mixture velocity and drift velocity used in Equation (46).

$$\alpha_c = \frac{1}{1 + \frac{P_i}{P_d}} \tag{49}$$

4.4. Evaluation of the Proposed Model

The proposed model demonstrates improved predictive accuracy, particularly in the high void fraction flows beyond the peak of the distribution parameter. This addresses a known issue identified in the studies by Godbole et al., where the accuracy of conventional models was fundamentally constrained by the assumption of a constant C_0 [3]. Furthermore, the standard DFM is subject to a non-physical limitation where the maximum calculable void fraction is $1/C_0$. The proposed C_0 model resolves this inconsistency while avoiding the computational complexity inherent in formulations such as the Chexal et al. model [47].

The proposed methodology was verified against a broad range of experimental data from multiple studies. The validation dataset encompassed diameters ranging from 1.27 to

15 cm, u_{sl} and u_{sg} ranging from 0 to 2.9 m/s and 0.009 to 42.9 m/s, respectively, and a full range of α_g from 0 to 1 [3,48–51].

To evaluate the proposed model, a comparative analysis was conducted against two established drift–flux correlations: the model of Nicklin et al. and that of Greskovich and Cooper [26,34]. While the Nicklin et al. model provides accurate results with a simple formulation, its use of a constant distribution parameter ($C_0 = 1.2$) makes it theoretically incapable of predicting void fractions exceeding 0.833 [26]. In contrast, the Greskovich and Cooper model, which employs $C_0 = 1.0$, can predict the full range of void fractions [34]. The performance of these three models was evaluated across seven distinct void fraction ranges using the Root Mean Squared Error (RMSE) and Mean Absolute Percentage Error (MAPE) as metrics, with the results presented in Tables 5 and 6, respectively. These two DFMs are not the most advanced models available, but their accuracy is relatively high considering their simplicity, and the reason for choosing them was to compare the results of the proposed model to two models with higher and lower values of C_0.

Table 5. Comparison of RMSE values in various void fraction ranges.

Void Fraction Range	Nicklin et al.	Greskovich and Cooper	Proposed Model
$0 < \alpha_g \leq 0.25$	0.022	0.035	0.015
$0.25 < \alpha_g \leq 0.5$	0.039	0.039	0.021
$0.5 < \alpha_g \leq 0.75$	0.036	0.108	0.030
$0.75 < \alpha_g < 1$	0.096	0.085	0.042
$0 < \alpha_g < 1/1.2$	0.031	0.085	0.029
$1/1.2 \leq \alpha_g < 1$	0.113	0.057	0.039
$0 < \alpha_g < 1$	0.066	0.078	0.032

Table 6. Comparison of MAPE values in various void fraction ranges.

Void Fraction Range	Nicklin et al.	Greskovich and Cooper	Proposed Model
$0 < \alpha_g \leq 0.25$	17.3%	28.5%	9.3%
$0.25 < \alpha_g \leq 0.5$	10.1%	9.3%	5.1%
$0.5 < \alpha_g \leq 0.75$	4.9%	13.2%	3.5%
$0.75 < \alpha_g < 1$	8.7%	8.1%	3.9%
$0 < \alpha_g < 1/1.2$	9.9%	19.0%	6.3%
$1/1.2 \leq \alpha_g < 1$	11.3%	4.8%	3.2%
$0 < \alpha_g < 1$	10.4%	14.9%	5.4%

The proposed approach demonstrates superior accuracy across all evaluated ranges. In the region where $\alpha_g < 0.75$, the Nicklin et al. model outperforms the Greskovich and Cooper model, while for $\alpha_g > 0.75$, the latter exhibits higher accuracy. Below the theoretical limit of $\alpha_g = 0.833$, the proposed model yields the best results, with the Nicklin et al. model showing comparable accuracy. However, for void fractions exceeding this limit, the accuracy of the Nicklin et al. model degrades significantly. In this high void fraction regime, the proposed approach remains the most accurate, achieving an RMSE of 0.039, with an overall total RMSE of 0.032 for the full range.

It is important to note that in the low void fraction regime ($\alpha_g < 0.25$), where all models exhibited their lowest performance, a small RMSE can correspond to a large MAPE. The improved performance of the proposed model is achieved while using a drift velocity correlation nearly identical to that of Nicklin et al.; the Greskovich and Cooper model, in contrast, utilizes a significantly higher drift velocity (1.92 times). In addition to its performance across void fraction ranges, the model's robustness was evaluated against

varying pipe diameters, with the results presented in Table 7. Both the Nicklin et al. and Greskovich and Cooper models show a clear degradation in accuracy with increasing pipe diameter. The proposed model, however, maintained a consistent level of accuracy across the entire range of diameters investigated. This robust performance suggests its suitability for applications involving a wide variety of pipe diameters.

Table 7. Comparison of MAPE values in different pipe diameters.

Diameter (m)	Nicklin et al.	Greskovich and Cooper	Proposed Model
$D \approx 0.01$	5.4%	13.2%	4.6%
$D \approx 0.05$	10%	10.2%	5.6%
$D \approx 0.15$	19%	31.2%	5.8%

Plotting calculated values against the experimental data in Figure 14 shows that the proposed model keeps the error of predictions consistent, while other models show a decline or improvements in a certain range. For instance, Nicklin et al.'s model shows its limitations on void fractions above 0.833, and Greskovich and Cooper model also exhibit higher errors on critical void fraction zones and lower void fractions. The accuracy of the results for various error bands is presented in Table 8 for ranges of acceptable errors. A total of 98.1% of estimations are in the 25% error range for the proposed model, which shows comparable accuracy to Nicklin et al.'s model. However, Greskovich and Cooper's approach has 83.2% of data within a 25% error band. The accuracy of other models becomes significantly lower than that of the proposed model when the acceptable error of predictions is set at 15%. The proposed model has 94.8% of data within a 15% error, while Nicklin et al. and Greskovich and Cooper models have 75.0% and 56.5% of data within that range, respectively. The differences become more apparent when acceptable errors are set to 5%, in which the proposed model has 64.8% data within that range, while both other models have approximately 29.5% of the data predicted within that range of accuracy.

Table 8. Comparison of the distribution of predicted values in various error bands.

Error Band	Nicklin et al.	Greskovich and Cooper	Proposed Model
$MAPE \leq 25\%$	96.4%	83.2%	98.1%
$MAPE \leq 20\%$	90.4%	70.6%	97.0%
$MAPE \leq 15\%$	75.0%	56.5%	94.8%
$MAPE \leq 10\%$	51.6%	41.5%	88.5%
$MAPE \leq 5\%$	29.4%	29.9%	64.8%

The proposed approach utilizes a two-range model to describe the non-monotonic behavior of C_0 as a function of α_c. The first component of the model, Equation (47a), describes the initial increase in C_0 to a peak value, which occurs at a void fraction consistent with experimental data and the published literature. The subsequent rapid decrease towards a limiting value of $C_0 = 1.0$ at high void fractions is modeled using the function of Equation (47b). This formulation effectively addresses the limitations inherent in constant distribution parameter assumptions while avoiding the computational complexity of iterative solution procedures. In summary, the first function covers void fractions up to the critical values observed by other studies, such as Chexal et al., and the second function covers extreme gas void fractions.

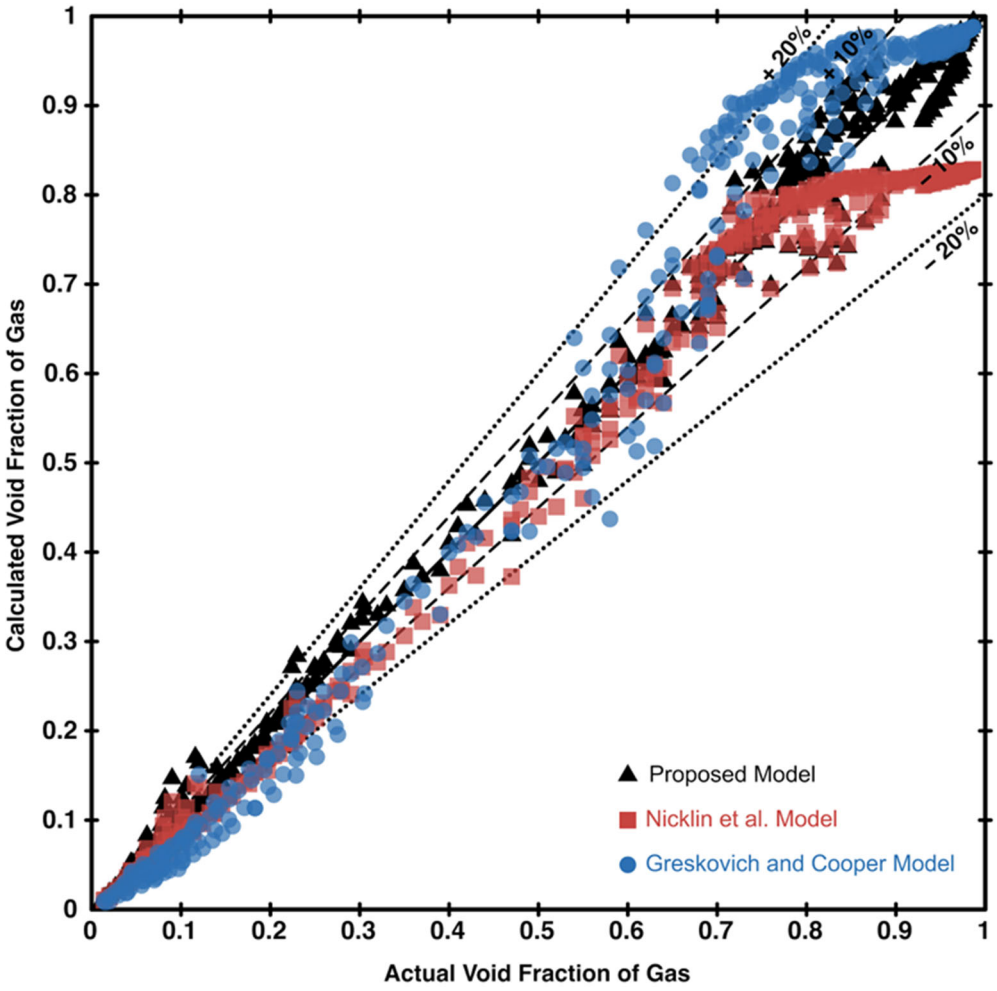


Figure 14. Calculated vs. actual void fraction of gas using the proposed model and two constant C_0 models, with error bands.

The maximum and minimum bounds used in the proposed model (C_{0MAX} and C_{0MIN}) and the coefficients can be further refined by incorporating established physical correlations. For example, it is well-established in the literature that the distribution parameter depends on the density contrast between the phases, generally decreasing as this difference diminishes, irrespective of the void fraction [36]. This principle can be directly applied to adjust the C_{0MAX} parameter to better reflect the specific fluid properties, such as density, like models offered by Liao et al., for the system under investigation [36]. Furthermore, higher values for C_{0MAX} can be considered when flow is in the laminar region which, according to previous studies, shows higher C_0 values [40,45,46].

Although variations of temperature are not explicitly parameterized in the original flow criteria, the proposed model captures these effects in long pipes when implemented within a computational grid, where the DFM and Taitel et al. assumptions remain valid locally. While this study extensively validates the model against experimental data for air–water systems across a wide range of diameters (1.27–15 cm), it is important to acknowledge that industrial gas lift operations often involve hydrocarbon fluids with higher viscosities and distinct interfacial tension properties. The fundamental drift–flux principles remain applicable, but the specific coefficients optimized here (λ_1 and λ_2) are currently calibrated for low-viscosity systems. Consequently, the structure of the proposed model is designed to be amenable to data analysis techniques and machine learning, which can be effectively employed to fine-tune these parameters using field data from high-pressure oil–gas wells to ensure robust industrial applicability.

5. Conclusions

This study aimed to improve the predictive accuracy of the gas void fraction for vertical upward flow, specifically pertaining to gas lift systems. The investigation was motivated by the need to overcome the deficiencies of existing correlations without resorting to computationally intensive models. A method was developed to estimate the void fraction based on main operational inputs (e.g., phase superficial velocities or mass flow rates) for defined, steady-state thermodynamic conditions. Additionally, new approaches for developing flow pattern maps based on mixture velocity and mass flow rate scenarios were presented. The outcomes of this research are as follows.

A novel flow pattern map was developed by integrating the drift–flux model with the Taitel et al. transition criteria. Its coordinate system, based on mixture and phase volumetric flow rates, enhances its utility for industrial applications, such as gas lift.

A methodology was established to predict flow pattern evolution in long vertical pipes with large pressure variations, using the known injected gas mass flow rate as the primary input.

A structurally consistent set of correlations was formulated to estimate both transition pressures and drift–flux parameters, enabling predictive modeling of flow patterns.

The effect of the gas void fraction on flow dynamics was observed as a single term called the distribution-weighted gas void fraction ($\alpha_c = \alpha_g C_0$), which was later utilized to introduce a void fraction estimation model.

Analysis of a broad experimental dataset revealed that the distribution parameter (C_0) exhibits a non-monotonic behavior, attaining a peak value at a gas void fraction (α_g) of approximately 0.73 (corresponding to $\alpha_c = 0.9$) before decreasing at higher void fractions.

Comparative analysis showed that the proposed model significantly outperforms both simpler and more complex models, achieving about twofold improvement in overall accuracy while maintaining a non-iterative, computationally efficient structure.

The proposed approach demonstrated robust performance across a wide range of pipe diameters, maintaining a consistent level of accuracy where conventional models often degrade, making it highly suitable for practical engineering applications, such as gas lift.

The proposed model assumptions are the same as the drift–flux model and the Taitel et al. model. However, when implemented within a numerical simulation that utilizes a high-resolution computational grid, this approach makes it possible to capture the effects of temperature and pressure variations throughout the flow domain while considering isothermal conditions for each computational cell.

The parametric and simpler structure of the proposed model made it possible to incorporate data analysis techniques for fine-tuning the proposed model to better fit the operating conditions and experimental data.

Author Contributions: Conceptualization, methodology, validation, and writing—original draft, O. Heydari; supervision, formal analysis, and review & editing, S. Butt and S. Zendehboudi; project administration and funding acquisition, S. Butt. All authors have read and agreed to the published version of the manuscript.

Funding: This research was funded by Novamera Inc., MITACS Accelerate, and the National Science and Engineering Research Council (NSERC) of Canada for the development and optimization of Surgical Mining Technology.

Institutional Review Board Statement: Not applicable.

Informed Consent Statement: Not applicable.

Data Availability Statement: There were no new data created for this study, and data used for verification and analysis were from the literature cited in the manuscript.

Conflicts of Interest: The authors declare no conflict of interest.

Nomenclatures

Acronyms	
FVM	Finite Volume Method
HEM	Homogeneous Equilibrium Model
CFD	Computational Fluid Dynamics
DFM	Drift–Flux Model
RMSE	Root Mean Squared Error
MAPE	Mean Absolute Percentage Error
AI	Artificial Intelligence
Letters/Symbols	
A	Cross-sectional area (m^2)
C_0	Distribution parameter (−)
C_{0A}	Assumed distribution parameter for the initial calculation of α_c (−)
C_{0L}	Proposed distribution parameter model for lower ranges of α_c (−)
C_{0H}	Proposed distribution parameter model for higher ranges of α_c (−)
C_F	Empirical variable in pressure functions (−)
D	Pipe diameter (m)
g	Acceleration due to gravity ($m.s^{-2}$)
k_1	Empirical constant of pressure functions (−)
k_2	Empirical constant of pressure functions (−)
k_3	Empirical constant of pressure functions (−)
l_i	Distance from inlet (m)
l_c	Required distance from inlet for the formation of slugs (m)
$\dot{m}$	Mass flow rate ($kg.s^{-1}$)
P	Pressure (Pa)
P_d	Drift pressure (Pa)
P_t	Flow pattern transition pressure (Pa)
Q	Volumetric flow rate ($m^3.s^{-1}$)
R_s	Specific gas constant ($m^2.s^{-2}.K^{-1}$)
Re	Reynolds number (−)
S	Slip ratio (−)
T	Temperature (K)
u	Velocity of phase ($m.s^{-1}$)
u_d	Drift velocity ($m.s^{-1}$)
$u_{m,C}$	Mixture velocity causing a collapse of the Taylor bubble at a point of interest ($m.s^{-1}$)
u_s	Superficial velocity of phase ($m.s^{-1}$)
V	Volume occupied by phase (m^3)
x	Gas quality (−)
Z	Compressibility factor of the gas phase (−)
α	Void fraction of phase (−)
α_c	Distribution-weighted void fraction (−)
α_{c0}	Inflection point for lower ranges of the proposed distribution parameter model (−)
β_g	Volumetric gas quality (−)
β_t	Volumetric gas quality at which the higher turbulent phase switches (−)
ε	Negligible positive value to ensure non-negative values (−)
λ_1	Coefficient for the proposed distribution parameter model (−)
λ_2	Coefficient for the proposed distribution parameter model (−)

https://doi.org/10.3390/fluids11010006

μ	Dynamic viscosity of the phase ($kg.m^{-1}.s^{-1}$)
v	Kinematic viscosity of the phase ($m^2.s^{-1}$)
ρ	Density of the phase ($kg.m^{-3}$)
σ	Surface tension between the gas and liquid phase ($kg.s^{-2}$)
ψ	Ratio of pressure to density of the gas phase ($m^2.s^{-2}$))
Subscripts	
g	Gas phase
i	Parameter value at the point of interest
l	Liquid phase
m	Mixture
t	Transition criteria
$t1$	Transition criteria for annular flow
$t2$	Transition criteria for bubbly/dispersed bubbly to slug/churn flow
$t3$	Transition criteria for churn to slug formation flow
$t4$	Transition criteria for bubbly to dispersed bubbly flow

References

1. Wang, Y.; Wang, Z. An Overview of Liquid–Vapor Phase Change, Flow and Heat Transfer in Mini-and Micro-Channels. *Int. J. Therm. Sci.* **2014**, *86*, 227–245. [CrossRef]
2. Igbokwe, L.C.; Naterer, G.F.; Zendehboudi, S.; Pedersen, S.; Jespersen, S. Suppression of Liquid Slugs and Phase Separation through Pipeline Bends. *Can. J. Chem. Eng.* **2022**, *100*, 1778–1795. [CrossRef]
3. Godbole, P.V.; Tang, C.C.; Ghajar, A.J. Comparison of Void Fraction Correlations for Different Flow Patterns in Upward Vertical Two-Phase Flow. *Heat Transf. Eng.* **2011**, *32*, 843–860. [CrossRef]
4. Starkman, E.S.; Schrock, V.E.; Neusen, K.F.; Maneely, D.J. Expansion of a Very Low Quality Two-Phase Fluid through a Convergent-Divergent Nozzle. *J. Basic Eng.* **1964**, *86*, 247–254. [CrossRef]
5. Butterworth, D. A Comparison of Some Void-Fraction Relationships for Co-Current Gas-Liquid Flow. *Int. J. Multiph. Flow* **1975**, *1*, 845–850. [CrossRef]
6. Fauske, H. Critical Two-Phase, Steam–Water Flows. In *Proceedings of the 1961 Heat Transfer and Fluid Mechanics Institute*; Stanford University Press: Stanford, CA, USA, 1961; pp. 79–89.
7. Zivi, S.M. Estimation of Steady-State Steam Void-Fraction by Means of the Principle of Minimum Entropy Production. *J. Heat Transfer.* **1964**, *86*, 247–251. [CrossRef]
8. Spedding, P.L.; Chen, J.J.J. Holdup in Two Phase Flow. *Int. J. Multiph. Flow* **1984**, *10*, 307–339. [CrossRef]
9. Hamersma, P.J.; Hart, J. A Pressure Drop Correlation for Gas/Liquid Pipe Flow with a Small Liquid Holdup. *Chem. Eng. Sci.* **1987**, *42*, 1187–1196. [CrossRef]
10. Chisholm, D. Pressure Gradients Due to Friction during the Flow of Evaporating Two-Phase Mixtures in Smooth Tubes and Channels. *Int. J. Heat Mass Transf.* **1973**, *16*, 347–358. [CrossRef]
11. Smith, S.L. Void Fractions in Two-Phase Flow: A Correlation Based upon an Equal Velocity Head Model. *Proc. Inst. Mech. Eng.* **1969**, *184*, 647–664. [CrossRef]
12. Sultan, R.A.; Rahman, M.A.; Rushd, S.; Zendehboudi, S.; Kelessidis, V.C. Validation of CFD Model of Multiphase Flow through Pipeline and Annular Geometries. *Part. Sci. Technol.* **2019**, *37*, 685–697. [CrossRef]
13. Heydari, O.; Sahraei, E.; Skalle, P. Investigating the Impact of Drillpipe's Rotation and Eccentricity on Cuttings Transport Phenomenon in Various Horizontal Annuluses Using Computational Fluid Dynamics (CFD). *J. Pet. Sci. Eng.* **2017**, *156*, 801–813. [CrossRef]
14. Zuber, N.; Findlay, J.A. Average Volumetric Concentration in Two-Phase Flow Systems. *J. Heat Transfer.* **1965**, *87*, 453–468. [CrossRef]
15. Wallis, G.B. *One-Dimensional Two-Phase Flow*; Courier Dover Publications: Mineola, NY, USA, 2020; ISBN 0-486-84282-7.
16. Ishii, M. *One-Dimensional Drift-Flux Model and Constitutive Equations for Relative Motion Between Phases in Various Two-Phase Flow Regimes*; Argonne National Lab.: Lemont, IL, USA, 1977.
17. Nepomnyashchikh, I.; Liburdy, J.A. Analysis of the Slip Relation Parameters in the Developing Region of Vertical Upward Two-Phase Flow With Co-Flowing Streams. In *Proceedings of the Fluids Engineering Division Summer Meeting, Philadelphia, PA, USA, 27–30 July 2025*; American Society of Mechanical Engineers: New York, NY, USA, 2025; Volume 89008, p. V002T07A024.
18. Hibiki, T.; Dong, C.; Tsukamoto, N. Full-Range Drift–Flux Correlation for Upward Cocurrent Two-Phase Flows in Vertical Pipes. *Int. J. Energy Res.* **2025**, *2025*, 6193526. [CrossRef]

19. Zhao, Q.; Hibiki, T. One-Dimensional Drift-Flux Correlation for Vertical Upward Two-Phase Flow in Large Size Concentric and Eccentric Annuli. *Int. J. Multiph. Flow* **2019**, *113*, 33–44. [CrossRef]
20. Chexal, B.; Lellouche, G. *Full-Range Drift-Flux Correlation for Vertical Flows*; Electric Power Research Inst.: Palo Alto, CA, USA, 1985.
21. Hibiki, T.; Ishii, M. Distribution Parameter and Drift Velocity of Drift-Flux Model in Bubbly Flow. *Int. J. Heat Mass Transf.* **2002**, *45*, 707–721. [CrossRef]
22. Ma, J.; Jin, N.-D.; Wang, D.-Y.; Liu, D.-Y.; Liu, W.-X. Measurement of Water Holdup in Vertical Upward High Water-Cut Oil-in-Water Flows Using a High Frequency Sensor. *Sens. Actuators A: Phys.* **2019**, *289*, 165–179. [CrossRef]
23. Song, K.; Hibiki, T. Two-Group Drift-Flux Model for Dispersed Gas-Liquid Flows in Medium-to-Large Pipes. *Int. J. Heat Mass Transf.* **2025**, *250*, 127274. [CrossRef]
24. Ghajar, A.J.; Tang, C.C. Void Fraction and Flow Patterns of Two-Phase Flow in Upward and Downward Vertical and Horizontal Pipes. In *Advances in Multiphase Flow and Heat Transfer: Volume 4*; Bentham Science Publishers: Sharjah, United Arab Emirates, 2012; pp. 175–201.
25. Sun, B.; Sun, L.C.; Xing, D.C.; Tian, D.G.; Liu, J.Y. A Study of the Application of Drift-Flux Model in Gas-Liquid Two-Phase Flow in a Large Tube. *J. Exp. Fluid Mech.* **2013**, *27*, 56–59.
26. Nicklin, D.J. Two-Phase Flow in Vertical Tube. *Trans. Instn. Chem. Engrs.* **1962**, *40*, 61–68.
27. Ghajar, A.J.; Tang, C.C. Advances in Void Fraction, Flow Pattern Maps and Non-Boiling Heat Transfer Two-Phase Flow in Pipes with Various Inclinations. In *Advances in Multiphase Flow and Heat Transfer: Volume 1*; Bentham Science Publishers: Sharjah, United Arab Emirates, 2009; pp. 1–52.
28. Zou, L.; Zhao, H.; Zhang, H. Newton-Krylov Method in Solving Drift-Flux Two-Phase Flow Problems for Both Pre-CHF and Post-CHF Conditions at Steady State. *Ann. Nucl. Energy* **2018**, *112*, 517–530. [CrossRef]
29. Rassame, S.; Hibiki, T. Drift-Flux Correlation for Gas-Liquid Two-Phase Flow in a Horizontal Pipe. *Int. J. Heat Fluid Flow* **2018**, *69*, 33–42. [CrossRef]
30. Dong, C.; Rassame, S.; Zhang, L.; Hibiki, T. Drift-Flux Correlation for Upward Two-Phase Flow in Inclined Pipes. *Chem. Eng. Sci.* **2020**, *213*, 115395. [CrossRef]
31. Hibiki, T.; Tsukamoto, N. Drift-Flux Model for Upward Dispersed Two-Phase Flows in Vertical Medium-to-Large Round Tubes. *Prog. Nucl. Energy* **2023**, *158*, 104611. [CrossRef]
32. Dong, S.; Hibiki, T. Modeling Axial Void Fraction Profile of Upward Subcooled Boiling Flows in Vertical Round Tubes. *Appl. Therm. Eng.* **2025**, *280*, 128309. [CrossRef]
33. Bonnecaze, R.H.; Erskine, W., Jr.; Greskovich, E. 1971 Holdup and Pressure Drop for Two-phase Slug Flow in Inclined Pipelines. *AIChE J.* **1971**, *17*, 1109–1113. [CrossRef]
34. Greskovich, E.J.; Cooper, W.T. Correlation and Prediction of Gas-liquid Holdups in Inclined Upflows. *AIChE J.* **1975**, *21*, 1189–1192. [CrossRef]
35. Jowitt, D.; Cooper, C.A.; Pearson, K.G. *The THETIS 80% Blocked Cluster Experiment. Part 1*; UKAEA Atomic Energy Establishment: Winfrith, UK, 1984.
36. Liao, L.H.; Parlos, A.; Griffith, P. *Heat Transfer, Carryover and Fall Back in PWR Steam Generators During Transients*; Massachusetts Inst. of Tech.: Cambridge, CA, USA, 1985.
37. Morooka, S.; Ishizuka, T.; Iizuka, M.; Yoshimura, K. Experimental Study on Void Fraction in a Simulated BWR Fuel Assembly (Evaluation of Cross-Sectional Averaged Void Fraction). *Nucl. Eng. Des.* **1989**, *114*, 91–98. [CrossRef]
38. Kokal, S.L.; Stanislav, J.F. An Experimental Study of Two-Phase Flow in Slightly Inclined Pipes—II. Liquid Holdup and Pressure Drop. *Chem. Eng. Sci.* **1989**, *44*, 681–693. [CrossRef]
39. Bestion, D. The Physical Closure Laws in the CATHARE Code. *Nucl. Eng. Des.* **1990**, *124*, 229–245. [CrossRef]
40. Fabre, J.; Liné, A. Modeling of Two-Phase Slug Flow. *Annu. Rev. Fluid Mech.* **1992**, *24*, 21–46. [CrossRef]
41. Taitel, Y.; Barnea, D.; Dukler, A.E. Modelling Flow Pattern Transitions for Steady Upward Gas-liquid Flow in Vertical Tubes. *AIChE J.* **1980**, *26*, 345–354. [CrossRef]
42. Nenes, A.; Assimacopoulos, D.; Markatos, N.; Mitsoulis, E. Simulation of Airlift Pumps for Deep Water Wells. *Can. J. Chem. Eng.* **1996**, *74*, 448–456. [CrossRef]
43. Saito, T.; Kajishima, T.; Tsuchiya, K. Pumping Characteristics of a Large-Scale Gas-Lift System. *Exp. Therm. Fluid Sci.* **2004**, *28*, 479–488. [CrossRef]
44. Shi, H.; Holmes, J.A.; Durlofsky, L.J.; Aziz, K.; Diaz, L.R.; Alkaya, B.; Oddie, G. Drift-Flux Modeling of Two-Phase Flow in Wellbores. *SPE J.* **2005**, *10*, 24–33. [CrossRef]
45. Fréchou, D. *Étude de l'écoulement Vertical Ascendant à Trois Fluides En Conduite Vertical*; INPT: Toulouse, France, 1986.
46. Mao, Z.-S.; Dukler, A.E. The Motion of Taylor Bubbles in Vertical Tubes—II. Experimental Data and Simulations for Laminar and Turbulent Flow. *Chem. Eng. Sci.* **1991**, *46*, 2055–2064. [CrossRef]

47. Chexal, B.; Lellouche, G.; Horowitz, J.; Healzer, J. A Void Fraction Correlation for Generalized Applications. *Prog. Nucl. Energy* **1992**, *27*, 255–295. [CrossRef]
48. Fernandes, R.C. *Experimental and Theoretical Studies of Isothermal Upward Gas-Liquid Flows in Vertical Tubes*; University of Houston: Houston, TX, USA, 1981.
49. Alamu, M.B. Investigation of Periodic Structures in Gas-Liquid Flow. Ph.D. Thesis, University of Nottingham, Nottingham, UK, 2010.
50. Hills, J.H. The Operation of a Bubble Column at High Throughputs: I. Gas Holdup Measurements. *Chem. Eng. J.* **1976**, *12*, 89–99. [CrossRef]
51. Liu, Y.; Luo, C.; Zhang, L.; Liu, Z.; Xie, C.; Wu, P. Experimental and Modeling Studies on the Prediction of Liquid Loading Onset in Gas Wells. *J. Nat. Gas Sci. Eng.* **2018**, *57*, 349–358. [CrossRef]

Disclaimer/Publisher's Note: The statements, opinions and data contained in all publications are solely those of the individual author(s) and contributor(s) and not of MDPI and/or the editor(s). MDPI and/or the editor(s) disclaim responsibility for any injury to people or property resulting from any ideas, methods, instructions or products referred to in the content.